



# A retrieval method for land surface temperatures based on UAV broadband thermal infrared images via the three-dimensional look-up table

Xue Zhong<sup>a</sup>, Lihua Zhao<sup>a</sup>, Jie Wang<sup>b</sup>, Xiang Zhang<sup>a</sup>, Zichuan Nie<sup>a</sup>, Yingtan Li<sup>b</sup>, Peng Ren<sup>a,\*</sup>

<sup>a</sup> State Key Laboratory of Subtropical Building Science, Department of Architecture, South China University of Technology, 510640, Guangzhou, China

<sup>b</sup> School of Geographic Sciences, China West Normal University, 637009, Nanchong, China



## ARTICLE INFO

### Keywords:

Land surface temperatures (LSTs)  
Unmanned aerial vehicles (UAVs)  
Three-dimensional look-up table (3DLUT)  
Broadband thermal imager  
Radiative transfer equation (RTE)

## ABSTRACT

Land surface temperatures (LSTs) represent a crucial parameter to characterize the urban thermal environment. Although numerous methods have been proposed to retrieve LSTs based on data from satellites or unmanned aerial vehicles (UAVs), challenges remain for acquiring precise pixel-level LSTs of highly heterogeneous urban surfaces on the micro scale. This study proposed a method of temperature retrieval for UAV-derived broadband thermal infrared images via a three-dimensional look-up table (TRUB-3DLUT) to retrieve LSTs of complicated urban surfaces. Based on radiative transfer between surfaces and the atmosphere, the method comprehensively quantified the impacts of radiation emitted by surfaces, wavelength, land surface emissivity (LSE) and atmospheric parameters on the retrieved LSTs. Then, the 3DLUT was directly used to generate the urban low-altitude atmospheric products and retrieve the LSTs via the UAV-derived images with a high-spatial resolution. Validations demonstrated that the retrieved LSTs were well-aligned with the *in-situ* LSTs and that the absolute differences were less than 1.5 K for sunlit surfaces with higher emissivity. The TRUB-3DLUT offered practical utility in reducing the uncertainty of the inputs in the radiative transfer equation and thus improving the accuracy of the retrieved LSTs. Therefore, such a method is envisioned as an effective tool for quantitatively analyzing the spatial variations of urban thermal environments on the micro scale.

## 1. Introduction

Land surface temperatures (LSTs) play a crucial role in the phenomena of surface urban heat islands [1–3] and energy exchanges between land surfaces and the atmosphere [4,5]. The LSTs of different surfaces are governed by factors such as meteorological parameters (e.g. radiation, air temperatures and wind speeds) [6,7] and material-related parameters (e.g. specific heat capacity, reflectivity and emissivity) [8–10], all of which vary on the spatiotemporal scale, especially for heterogeneous urban surfaces [11,12]. In this regard, the availability of satellite data enables easy access to the spatiotemporal distribution of the LSTs on the large scale [13–15]. Accordingly, numerous LST-retrieval methods have been proposed based on the characteristics of thermal infrared (TIR) data, which can be classified into single-channel and multi-channel algorithms [16]. One commonality between such methods is that they require the input parameters of land surface emissivity (LSE), atmospheric parameters and effective wavelength [17–19]. However, the spatial resolutions of satellite data (e.g. Landsat 8, ASTER and MODIS) [20–22] or atmospheric products (e.g.

ERA5 and NCEP) [23–25] are too low to allow accurate LST-retrieval for heterogeneous urban surfaces, especially on the micro scale.

The use of unmanned aerial vehicles (UAVs) has enabled low-cost spatiotemporal LST-measurements through UAV-mounted, lightweight thermal imagers [26–30]. Such thermal imagers generally yield TIR images in TIFF or R-JPEG formats, showing the digital number and the RGB of each pixel. Nonetheless, some shortcomings are noteworthy. While manufacturers provide the calibration formula between the digital number and the at-sensor brightness temperature ( $T_{sensor}$ ), this does not represent a reliable method to accurately obtain  $T_{sensor}$  of outdoor environment from raw images with the TIFF format, given the temperature drift caused by unstable meteorological factors [31,32]. The R-JPEG format is specifically provided by the FLIR, which records the realistic  $T_{sensor}$  in a non-destructive and encrypted way and reads the  $T_{sensor}$  of each image via the FLIR Tools software (FLIR Systems, Inc., Wilsonville, OR, USA) [33,34]. Currently, no conversion formulae between the RGB and the  $T_{sensor}$  are available, and thus it is infeasible to obtain the  $T_{sensor}$  in batches and generate the orthophoto of  $T_{sensor}$  from raw images of the R-JPEG format. To obtain accurate LSTs via the UAV-mounted thermal imagers without considering the impacts of

\* Corresponding author.

E-mail addresses: [201920104230@mail.scut.edu.cn](mailto:201920104230@mail.scut.edu.cn) (X. Zhong), [arpren@scut.edu.cn](mailto:arpren@scut.edu.cn) (P. Ren).

## Nomenclature

LSTs	land surface temperatures
TIR	thermal infrared
LSE	land surface emissivity
UAVs	unmanned aerial vehicles
$T_{sensor}$	at-sensor brightness temperature (K)
$T_s$	surface temperature (K)
$T_{retrieved}$	retrieved $T_s$ (K)
$T_{measured}$	measured $T_s$ on the ground via the contact thermometers
RTE	radiative transfer equation
APs	atmospheric profiles
TRUB-3DLUT	temperature retrieval for UAV broadband TIR images via the three-dimensional look-up table
$T_a$	near-ground air temperature (K)
$RH$	near-ground relative humidity (%)
$B_\lambda(T_{sensor})$	at-sensor spectral radiance ( $W \cdot m^{-2} \cdot \mu m^{-1} \cdot sr^{-1}$ )
$B_\lambda(T_s)$	spectral radiance emitted from the blackbody at the temperature of $T_s$ ( $W \cdot m^{-2} \cdot \mu m^{-1} \cdot sr^{-1}$ )
$B_\lambda^{\dagger}, B_\lambda^{\downarrow}$	atmospheric upwelling and downwelling spectral radiances ( $W \cdot m^{-2} \cdot \mu m^{-1} \cdot sr^{-1}$ )
$\epsilon_\lambda$	spectral LSE
$\tau_\lambda$	spectral atmospheric transmittance
SRF/ $f(\lambda)$	spectral response function

$\lambda_e$	effective wavelength ( $\mu m$ )
$B_{\lambda_e}(T_{sensor})$	at-sensor radiance at the $\lambda_e$ ( $W \cdot m^{-2} \cdot \mu m^{-1} \cdot sr^{-1}$ )
$B_{\lambda_e}^{\dagger}, B_{\lambda_e}^{\downarrow}$	atmospheric upwelling and downwelling radiances at the $\lambda_e$ ( $W \cdot m^{-2} \cdot \mu m^{-1} \cdot sr^{-1}$ )
$\epsilon_{\lambda_e}$	LSE at the $\lambda_e$
$\tau_{\lambda_e}$	atmospheric transmittance at the $\lambda_e$
$\lambda_1, \lambda_2$	the lowest and highest point of the SRF range ( $\mu m$ )
NDVI	normalized difference vegetation index
$\rho_R, \rho_{NIR}$	reflectance values in the red and near-infrared bands
$\epsilon_{bb}$	broadband emissivity (8–14 $\mu m$ )
$B_{\lambda_e}'(T_{sensor})$	at-sensor radiance referred by the 3DLUT ( $W \cdot m^{-2} \cdot \mu m^{-1} \cdot sr^{-1}$ )
$B_i^{\dagger}, \tau_j^{\downarrow}$	atmospheric upwelling radiance and transmittance referred by the 3DLUT at the serial number of $i$ and $j$ ( $W \cdot m^{-2} \cdot \mu m^{-1} \cdot sr^{-1}$ )
$T_k$	surface temperature (K) referred by 3DLUT at the serial number of $k$
$R^2$	coefficient of determination
RMSE	root mean squared error
$R$	correlation coefficient
$T_{read}$	temperature readings of the single TIR image via the FLIR Tools software

$T_{sensor}$ , researchers have adapted empirical models for the digital number of TIR images and the measured surface temperature on the ground ( $T_{measured}$ ) [31,33,35,36]. However, despite the easy implementation of empirical line calibration, such calibration disregards the actual process of thermal radiative transfer, thus compromising the precision of the retrieved temperature ( $T_{retrieved}$ ).

To consider the actual process of thermal radiative transfer and improve the accuracy of retrieved surface temperatures, a few studies about remote sensing have attempted to reduce the uncertainty of input parameters in the radiative transfer equation (RTE). The studies about the sensitivity of the LST-retrieval models based on remote sensing have been analyzed (Fig. 1), which ranked the factors according to their importance. Against this background, crucial factors include the LSE, brightness temperatures, atmospheric parameters and wavelength. Firstly, LSE denotes a key parameter for retrieving LSTs: a deviation of 1% for the LSE could lead to an error of about 0.4 K–1 K for the retrieved LSTs [37–42]. Additionally, the atmosphere attenuates the radiance that emits from the surface and reaches the sensor, which further affects the brightness temperatures and LSTs. A deviation of 0.03  $W \cdot m^{-2} \cdot \mu m^{-1} \cdot sr^{-1}$  could result in errors in LSTs of 0.7 K in a dry

atmosphere and 1.1 K in a humid atmosphere [43–45]. Lastly, the determination of effective wavelengths may also lead to small errors in  $T_{retrieved}$ : variations in the wavelengths by several millimeters could cause deviations for LSTs that were less than 1.0 K [46–48]. Such literature has demonstrated the need to accurately obtain input parameters in the RTE for retrieving LSTs; however, no studies have hitherto comprehensively quantify the effects of  $T_{sensor}$ , LSE, atmospheric parameters and wavelength on  $T_{retrieved}$  from low-altitude UAV-derived images with a high-spatial-resolution.

To solve the RTE with multiple parameters, the use of the look-up table has been introduced. As a method based on iterative optimization, the look-up table pre-establishes the metric of similarity between the retrieved parameters and observed data, then determines the parameters in the table that are most similar to the observed data, and lastly records them [49–51]. Generally, the resolution (i.e. ranges and the step sizes) of the look-up table is defined by the empirical or measured values of the retrieved parameters [52,53]. The look-up table discretizes the continuous RTE, and the resolution is the sampling density of the parameters in the discretization process, which is crucial to the retrieved accuracy. The use of the look-up table reduces the uncertainty of  $T_{retrieved}$  caused by the inaccuracy of effective wavelengths [47]. Additionally, it has been used to invert parameters that were challenging to obtain in the complex RTE (the dimension of the look-up table depends on the number of retrieved parameters [54,55]). In this study, it was challenging to obtain both the precise effective wavelength of the thermal imager and the pixel-level atmospheric parameters and surface temperatures. Accordingly, a multiple-dimensional look-up table was employed to reduce the impacts of uncertain inputs on the  $T_{retrieved}$  and further accurately retrieve the LSTs.

Against this background, this study proposed a method based on UAV broadband TIR images via the three-dimensional look-up table to retrieve LSTs of complex urban surfaces. With field testing, employment of a three-dimensional look-up table (3DLUT) and validations, this method retrieved the pixel-scale urban surface temperatures with high heterogeneity to not only minimize the uncertainty of the inputs in the RTE but also improve the accuracy of  $T_{retrieved}$ .

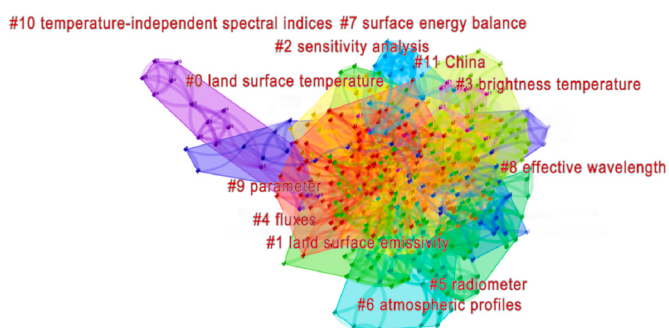


Fig. 1. The cluster chart about the sensitivity analysis of the LST-retrieval models based on remote sensing.

## 2. Methodology

### 2.1. Proposal of a method

The workflow of temperature retrieval for UAV broadband TIR images via the three-dimensional look-up table (TRUB-3DLUT) comprised four parts (Fig. 2), as follows:

Part I: The orthophoto of  $T_{sensor}$  was obtained based on processed TIR images and the proposed multivariate linear model in this study. Subsequently, the at-sensor radiance was calculated based on Planck's equation.

Part II: The pixel-wise emissivity was retrieved and validated based on processed multispectral images and the empirical model.

Part III: The approximate ranges of low-altitude (100 m) atmospheric parameters were obtained based on the proposed functions in this study. Based on the sensitivity analysis of the at-sensor radiance to three atmospheric parameters, the atmospheric downwelling radiance was fixed, and the pixel-level atmospheric upwelling radiance and transmittance were retrieved based on the 3DLUTs.

Part IV: Given the known at-sensor radiance, emissivity and atmospheric parameters, the LSTs were retrieved and validated based on the 3DLUTs.

A notable aspect was that this method could retrieve urban spatial LSTs via UAVs based on the actual process of radiative transfer, which provided a novel solution to the following hitherto unresolved challenges: (1) how to obtain at-sensor radiance from UAV-derived TIR images without accurate outdoor calibration parameters; (2) how to generate urban low-altitude atmospheric products with a high spatial resolution; (3) how to accurately retrieve pixel-level LSTs via the low-altitude sensing and analyze the sensitivity of  $T_{retrieved}$ .

### 2.2. Study area and measurements

The study area was the Science and Technology Park in the Guangdong Province in southern China, which covered an area of around

20000  $m^2$  (Fig. 3). Given its geographical location in the subtropical monsoon climate zone, the weather was hot and humid. Typical underlying surfaces in the park included tiles and grasses.

The datasets used in this study were divided into three parts: UAV images, ground measurements and APs. For UAV measurements, a multispectral camera (Micasense RedEdge-MX) and a thermal imager (FLIR XT2) were mounted on a DJI M300 RTK with a double gimbal. This set-up enabled the concurrent capturing of multispectral and TIR images via a synchronous control program developed by payload SDK (Fig. 4a). For ground measurements, a 102F portable Fourier transform thermal infrared spectrometer was employed to collect the emissivity spectra of underlying surfaces in flight (Fig. 4b) and some contact thermometers (i.e. HOBO TMC6-HE) were used to measure the thermodynamic temperature on the ground (This protocol was adopted from the literature [56].). Besides, four-component radiometers (i.e. KIPP-ZONE CMP3 and CGR3) and other sensors (i.e. HOBO MX2302A) were used to simultaneously obtain the shortwave and longwave radiations of the sky and typical underlying surfaces, air temperature ( $T_a$ ), relative humidity ( $RH$ ) and wind speed proximal to the ground (Fig. 4c). (The instruments are detailed in Appendix A.1). Lastly, for APs, ERA5 hourly reanalysis data covering the test area were used [57,58].

Considering the accuracy and stability of the spectra and LSTs, the tests were conducted at noon on a clear day. Before the flight, both multispectral and TIR cameras were preheated for half an hour to achieve thermal equilibrium. To minimize temporal variations of the LSTs caused by solar positions and environmental conditions during the test period, the flight time was limited to 12 min (13:18–13:30). At a height of 100 m, the UAV-mounted multispectral camera and the thermal imager continuously took images at 2.5-s intervals. Simultaneously, the emissivity spectra of the typical surfaces in the survey area were collected: 6 spectra of tiles under different lighting conditions and 2 spectra of sunlit grasses were obtained, for each of which the collection time was about 3 min. Furthermore, considering the heterogeneity on the ground and the possible effects of underlying surfaces (i.e. their nature and layout) on the near-ground meteorological parameters, the

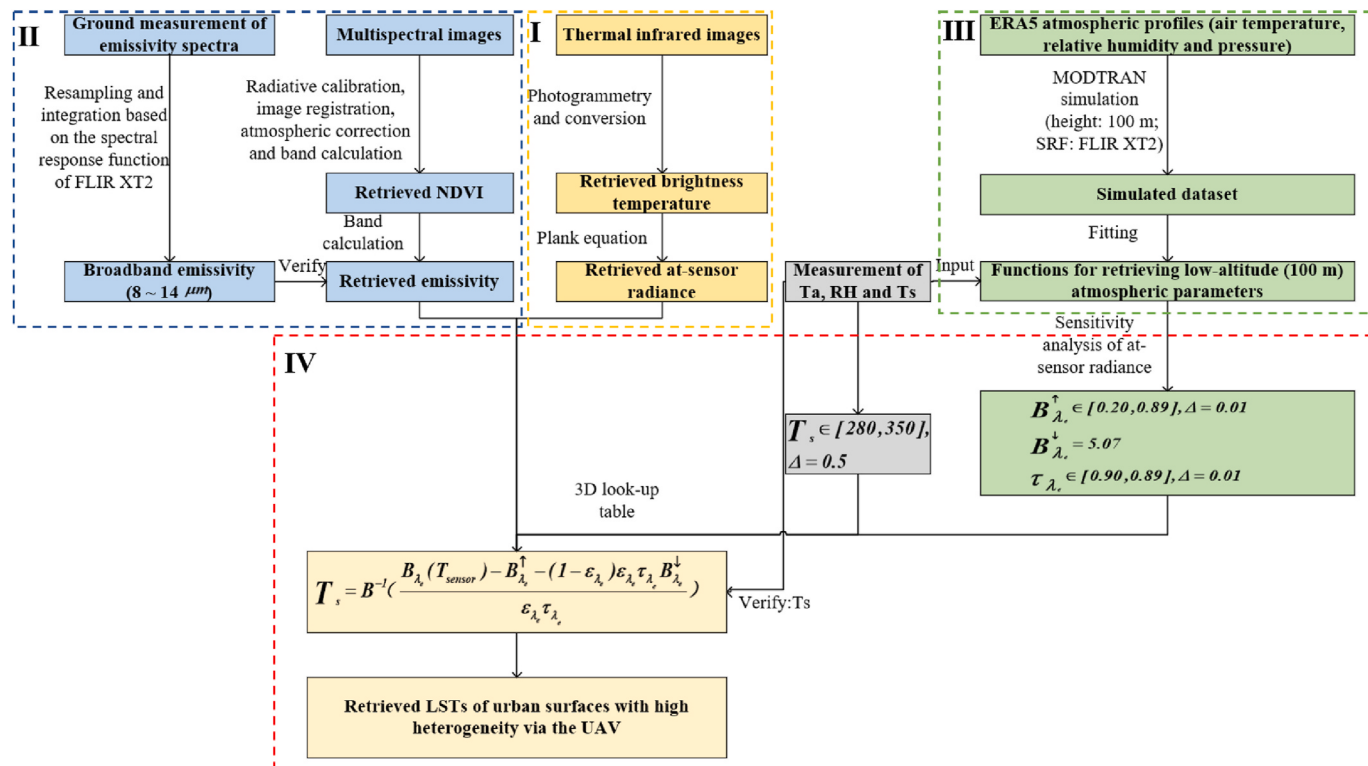


Fig. 2. The workflow of the TRUB-3DLUT for retrieving LSTs of heterogeneous urban surfaces.

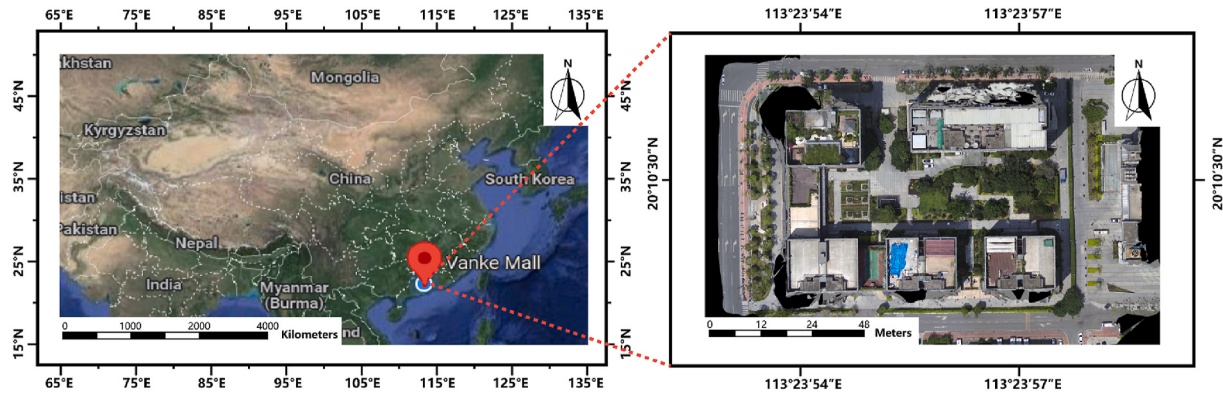


Fig. 3. The location of the study area.

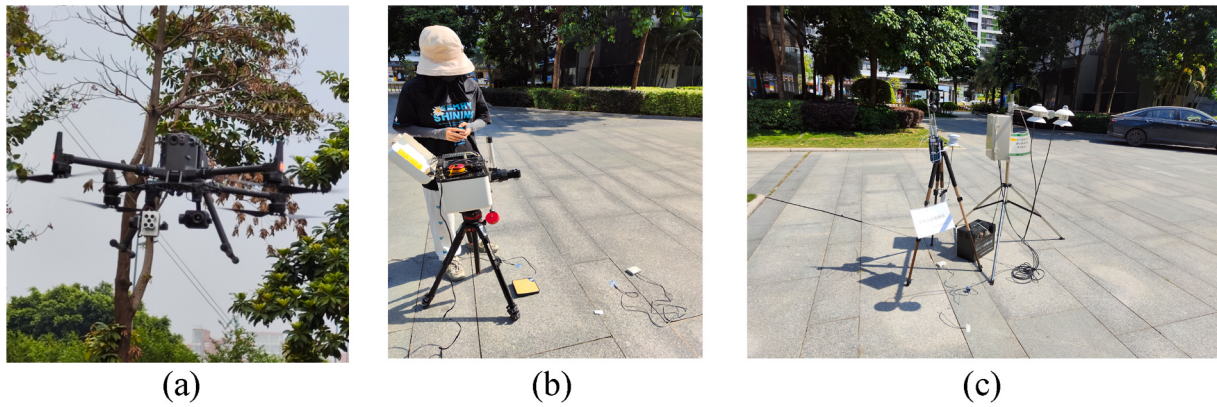


Fig. 4. Instruments used in this study.

points of  $T_{measured}$  and  $T_a/RH$  were evenly distributed in the study area. In total, 16 points were selected to measure the surface temperatures and to verify the retrieved LSTs. Additionally, 12 points were adopted to measure the  $T_a$  and  $RH$  for estimating the ranges of low-altitude atmospheric parameters across the area.

### 2.3. Theoretical basis

The spectral radiance received by the thermal imager (FLIR XT2) comprised three parts (Fig. 5): radiance emitted by the surfaces after atmospheric attenuation, atmospheric downwelling radiance reflected

by the surfaces after atmospheric attenuation, and atmospheric upwelling radiance.

The whole process can be expressed as follows [16,47]:

$$B_\lambda(T_{sensor}, \lambda) = B_\lambda(T_s, \lambda)\varepsilon_\lambda\tau_\lambda + (1 - \varepsilon_\lambda)B_\lambda^{\downarrow}\tau_\lambda + B_\lambda^{\uparrow} \quad (1)$$

where  $T_{sensor}$  is the at-sensor brightness temperature of surfaces ( $K$ ),  $T_s$  is the surface temperature ( $K$ ) that can be directly measured on the ground via contact thermometers,  $\lambda$  is the wavelength ( $\mu m$ ),  $\varepsilon_\lambda$  is the spectral LSE and  $\tau_\lambda$  is the spectral atmospheric transmittance.  $B_\lambda(T_{sensor}, \lambda)$  is the at-sensor spectral radiance ( $W \cdot m^{-2} \cdot \mu m^{-1} \cdot sr^{-1}$ ),  $B_\lambda(T_s, \lambda)$  is the spectral radiance emitted by surfaces at the temperature of

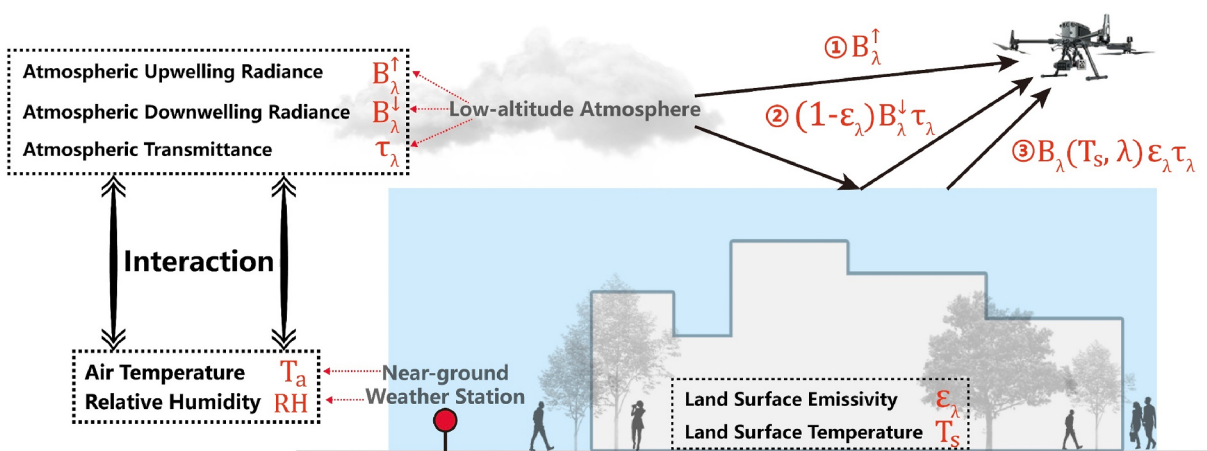


Fig. 5. The exhibition of thermal radiative transfer.

$T_s$  ( $W \cdot m^{-2} \cdot \mu m^{-1} \cdot sr^{-1}$ ),  $B_\lambda^1$  is the atmospheric downwelling spectral radiance and  $B_\lambda^\dagger$  is the atmospheric upwelling spectral radiance ( $W \cdot m^{-2} \cdot \mu m^{-1} \cdot sr^{-1}$ ).

The at-sensor radiance at a certain wavelength was calculated through Eq. (1), and the whole radiance received by the sensor needed to be integrated based on the range of spectral response function (SRF) of the FLIR XT2. However, this integration reduced the computational speed for retrieving LSTs, especially for UAV images with numerous pixels. To address this computational challenge, the whole range of the sensor's SRF was replaced by its effective wavelength (Eq. (2)) [46], at which the LSTs retrieval would then require five inputs (Eq. (3)). Nonetheless, the use of the effective wavelength represented an estimation method based on the line-by-line algorithm, which introduced errors of retrieved LSTs. For satellite sensors with a narrower-range SRF (i.e. almost within 1  $\mu m$ ), such errors would be negligible. Conversely, for UAV sensors with a wider-range SRF (e.g. 8–14  $\mu m$ ) [59], the uncertainty arising from this approximation algorithm was more substantial and thus not negligible. Against this background, this study proposed the look-up table to reduce the uncertainty of retrieved LSTs caused by the effective wavelength of broadband thermal imagers.

$$\lambda_e = \frac{\int_{\lambda_1}^{\lambda_2} \lambda f(\lambda) d\lambda}{\int_{\lambda_1}^{\lambda_2} f(\lambda) d\lambda} \quad (2)$$

$$T_s = B^{-1} \left( \frac{B_{\lambda_e}(T_{sensor}) - B_{\lambda_e}^\dagger - (1 - \varepsilon_{\lambda_e}) \varepsilon_{\lambda_e} \tau_{\lambda_e} B_{\lambda_e}^1}{\varepsilon_{\lambda_e} \tau_{\lambda_e}} \right) \quad (3)$$

where  $f(\lambda)$  is the SRF of the thermal imager,  $\lambda_1 \sim \lambda_2$  is the range of SRF (FLIR XT2: 8.0–14.0  $\mu m$ ),  $\lambda_e$  is the effective wavelength and  $B^{-1}$  is the inverse form of Planck's equation.

## 2.4. Data processing

### 2.4.1. Acquisition of at-sensor brightness temperature and at-sensor radiance

To solve the at-sensor radiance ( $B_{\lambda_e}(T_{sensor})$ ) in Eq. (3), the at-sensor brightness temperature must be obtained first. As the raw TIR images collected by FLIR XT2 were colored images in the R-JPEG format, which were displayed in RGB and encoded and encrypted  $T_{sensor}$ , it is necessary to propose a method to generate the orthophoto of  $T_{sensor}$ . In this study, the  $T_{sensor}$  of all images was read pixel by pixel through the interface of "unpack" provided by "flyr" (<https://bitbucket.org/nimmerwoner/flyr/src/master/>). As the temperature scale was unique to each image (i.e. the same RGB might correspond to different  $T_{sensor}$  in different images), it was necessary to unify the temperature scale. The statistics determined a range in which the 95% and above values were concentrated. Accordingly, the temperature scale of all images was processed such that it could be uniformly represented by the same palette. Upon unification of this scale for all images, the RGB values of stretched or compressed images corresponding to the unique  $T_{sensor}$  were read pixel by pixel; then the RGB values and  $T_{sensor}$  of all pixels were then subjected to black-box training and testing. Based on random division, 80% of pixels were used to train the conversion model, and the remaining 20% were used to validate the model:

$$T_{sensor} = a * R + b * G + c * B + d \quad (4)$$

where  $R$ ,  $G$  and  $B$  are values of three channels of the TIR images upon unification of the temperature scale, while  $a$ ,  $b$ ,  $c$  and  $d$  are fit coefficients.

This was followed by the placement of the processed TIR images into the photogrammetry software "ContextCapture" for producing the orthophoto of RGB values through numerous steps as follows: correction of camera distortion, alignment of images, extraction of feature points, geo-referencing of control points, constructions of high-density point clouds, reconstructions of the orthophoto and the digital surface model

[60–62]. Lastly, the ENVI software was applied to convert the pixel-scale RGB values into  $T_{sensor}$  through Eq. (4).

Upon obtaining at-sensor brightness temperature, the at-sensor radiance at the effective wavelength (Eq. (2)) could be calculated according to Planck's function [46]:

$$B_{\lambda_e}(T_{sensor}) = \frac{c_1}{\lambda_e^5 \cdot \left( e^{c_2 / \lambda_e T_{sensor}} - 1 \right)} \quad (5)$$

where  $c_1 = 1.191 \times 10^8 W \cdot m^{-2} \cdot sr^{-1} \cdot \mu m^{-4}$ ,  $c_2 = 14388 \mu m \cdot K$ .

### 2.4.2. Estimation and validation of pixel-wise LSE

To solve the emissivity in Eq. (3), the empirical model [63] was used. Since the model (Eq. 7) was established based on typical underlying surfaces in Guangzhou (including those in this study) [63], it was reasonably applied to retrieve pixel-scale emissivity. The model was established according to the strong correlation between LSE and NDVI, as calculated according to Eq. 6.

$$NDVI = (\rho_{NIR} - \rho_R) / (\rho_{NIR} + \rho_R) \quad (6)$$

where  $\rho_{NIR}$  and  $\rho_R$  refer respectively to the reflectance values in the near-infrared and red bands.

It was necessary that reflectance values should first be obtained accurately in the near-infrared and red bands. The reflectance orthophoto of the study area in five bands (Appendix A.1) was obtained after preprocessing raw multispectral images obtained by the Micasense RedEdge-MX, including photogrammetry processes, calibration of the whiteboard and band stacking via the Pix4D and ENVI software [64–66]. Then, the NDVI orthophoto was obtained based on the band calculation of the reflectance orthophoto; the LSE was retrieved after obtaining the NDVI (Eq. 7).

$$\begin{cases} LSE = 1.705 * NDVI + 0.902, & 0.00 \leq NDVI \leq 0.05 \\ LSE = 0.001 * \ln(NDVI) + 0.975, & 0.05 < NDVI \leq 1.00 \end{cases} \quad (6)$$

The model (Eq. 7) was established based on the sunlit surfaces, while some underlying surfaces in this study were in shadow because of the relative position between buildings and the sun. The distinctive lighting condition needs to further validate the effectiveness of the emissivity-retrieval model (Eq. 7). Therefore, the retrieved emissivity was compared with the measured emissivity obtained from resampling and integrating of the eight ground-measured emissivity spectra based on the SRF of FLIR XT2 (Eq. (8)). The absolute differences between retrieved emissivity and measured emissivity for those 8 points were calculated.

$$\varepsilon_{bb} = \frac{\int_{\lambda_1}^{\lambda_2} \varepsilon_\lambda B_\lambda(T_s, \lambda) f(\lambda) d\lambda}{\int_{\lambda_1}^{\lambda_2} B_\lambda(T_s, \lambda) f(\lambda) d\lambda} \quad (8)$$

where  $\varepsilon_{bb}$  is the broadband (8–14  $\mu m$ ) emissivity estimated from the spectral emissivity based on SRF of FLIR XT2 [67,68].

### 2.4.3. Estimation of low-altitude atmospheric parameters

To determine the atmospheric parameters in Eq. (3), the near-ground air temperature and relative humidity were selected as the representative near-ground meteorological data. The underlying rationale was that, given the flight height of the UAV of only 100 m, the lower-altitude atmospheric parameters were expected to closely approximate the near-ground meteorological data [47]. The air temperature would critically determine the radiance emitted by the atmosphere, and the water vapor content mainly absorbed the radiance in the TIR region.

The ERA5, as the highest spatiotemporal resolution of freely public atmospheric profiles, was initially served as the input to simulate the model for predicting atmospheric parameters at the height of 100 m above the larger area. Combined with the location of the test area and the flight time, the profiles of air temperature, relative humidity and

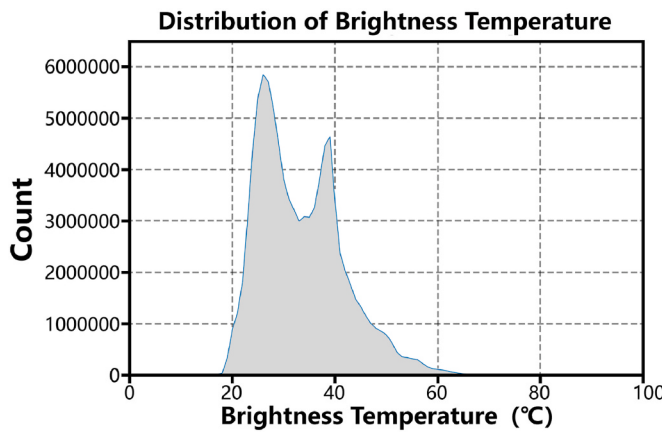


Fig. 6. The distribution of  $T_{\text{sensor}}$  collected by FLIR XT2.

pressure at 13:00 and 14:00 were downloaded (<https://www.ecmwf.int/en/forecasts/datasets/reanalysis-datasets/era5>). To simulate the low-altitude atmospheric parameters under various atmospheric conditions, the profiles from March to May were selected as the input for simulation. Such profiles were then entered into the MODTRAIN for simulation, with a simulated height of 100 m and then the SRF of FLIR XT2. A simulated dataset ( $n = 166$ ) was established, and binary quadratic functions were used to fit simulated atmospheric parameters at the height of 100 m and air temperature and relative humidity at the pressure level of 1000 hPa referred from the ERA5. Finally, the Levenberg-Marquardt method and the general global optimization method [69,70] were used to obtain the optimal fitting coefficients of the functions (Eq. (9)). Given the small size of the dataset, the bootstrap method [71] was used to evaluate the functions.

$$\begin{cases} B_{\lambda_e}^{\dagger} = a1T_a^2 + a2RH^2 + a3T_a \cdot RH + a4T_a + a5RH + a6 \\ B_{\lambda_e}^{\downarrow} = b1T_a^2 + b2RH^2 + b3T_a \cdot RH + b4T_a + b5RH + b6 \\ \tau_{\lambda_e} = c1T_a^2 + c2RH^2 + c3T_a \cdot RH + c4T_a + c5RH + c6 \end{cases} \quad (9)$$

where  $B_{\lambda_e}^{\dagger}$ ,  $B_{\lambda_e}^{\downarrow}$  and  $\tau_{\lambda_e}$  are atmospheric upwelling radiance, atmospheric downwelling radiance and atmospheric transmittance;  $a1 \sim a6$ ,  $b1 \sim b6$  and  $c1 \sim c6$  are fitting coefficients from the simulated dataset.

As the horizontal resolution of ERA5 atmospheric profiles was 27 km, the predicted results represented the average atmospheric condition of the larger area instead of the specific area in this study. Given factors such as complicated urban structures, heterogeneous surfaces and

human activities, the atmospheric conditions of different urban groups would vary, especially for the lower altitudes. It was thus crucial to substitute the measured  $T_a$  and  $RH$  into Eq. (9) for estimating the ranges of  $B_{\lambda_e}^{\dagger}$ ,  $B_{\lambda_e}^{\downarrow}$  and  $\tau_{\lambda_e}$  at the UAV height above the test area.

#### 2.4.4. Retrieval of LSTs based on 3DLUT and validation

Although the ranges of atmospheric parameters were determined, four unknowns of each pixel remained in the RTE ( $B_{\lambda_e}^{\dagger}$ ,  $B_{\lambda_e}^{\downarrow}$ ,  $\tau_{\lambda_e}$  and  $T_s$ ). Compared with the 3DLUT, the calculation amount of the four-dimensional look-up table was doubled. To address the computational challenge and quicken the process, one parameter needed to be fixed, such that only three unknowns could be expressed as parameters for the 3DLUT at any one time. Considering the sky clearness of the test period, the atmospheric parameters across the test area tended to be stable, so one of them could be fixed. Based on the control variable method, the sensitivity of at-sensor radiance to three atmospheric parameters was analyzed (Eq. (10)), and the atmospheric parameter that had the least effect on at-sensor radiance was fixed.

$$\Delta B_{\lambda_e}(T_{\text{sensor}}) = |B_{\lambda_e}(T_{\text{sensor}})(x + \Delta x) - B_{\lambda_e}(T_{\text{sensor}})(x)| \quad (10)$$

where  $\Delta B_{\lambda_e}(T_{\text{sensor}})$  is the variation of the at-sensor radiance,  $x$  is the three atmospheric parameters,  $\Delta x$  is the uncertainty of this input.  $B_{\lambda_e}(T_{\text{sensor}})(x)$  and  $B_{\lambda_e}(T_{\text{sensor}})(x + \Delta x)$  respectively denote values of at-sensor radiance for  $x$  and for  $x + \Delta x$ .

Upon fixing one atmospheric parameter, the 3DLUT was established to retrieve the pixel-scale LST and two other low-altitude atmospheric parameters from the orthophoto of the at-sensor radiance. Then, a mapping relationship  $f()$  between the unknowns and the 3DLUT-referred at-sensor radiance  $B'_{\lambda_e}(T_{\text{sensor}})$  was established (Eq. (11)). The ranges and step sizes of the atmospheric parameters in the 3DLUT were defined based on the expansion of the results of Eq. (9), whereas the range and step size of  $T_{\text{retrieved}}$  were determined by estimated LSTs of the test area during the flight. Accordingly, the serial number of the optimal referred radiance  $B'_{\lambda_e}(T_{\text{sensor}})$  of each pixel was obtained based on the minimum distance between  $B'_{\lambda_e}(T_{\text{sensor}})$  and  $B_{\lambda_e}(T_{\text{sensor}})$  (Eq. (12)). Hence, the corresponding variables under the serial numbers were retrieved for each pixel. To further verify the accuracy of the retrieved LSTs, the measured temperatures of 16 points were compared with the corresponding  $T_{\text{retrieved}}$  on the image.

$$B'_{\lambda_e}(T_{\text{sensor}}) = f(B_{\lambda_e}^{\dagger}, \tau_{\lambda_e}, T_{\text{retrieved}}) \quad (11)$$

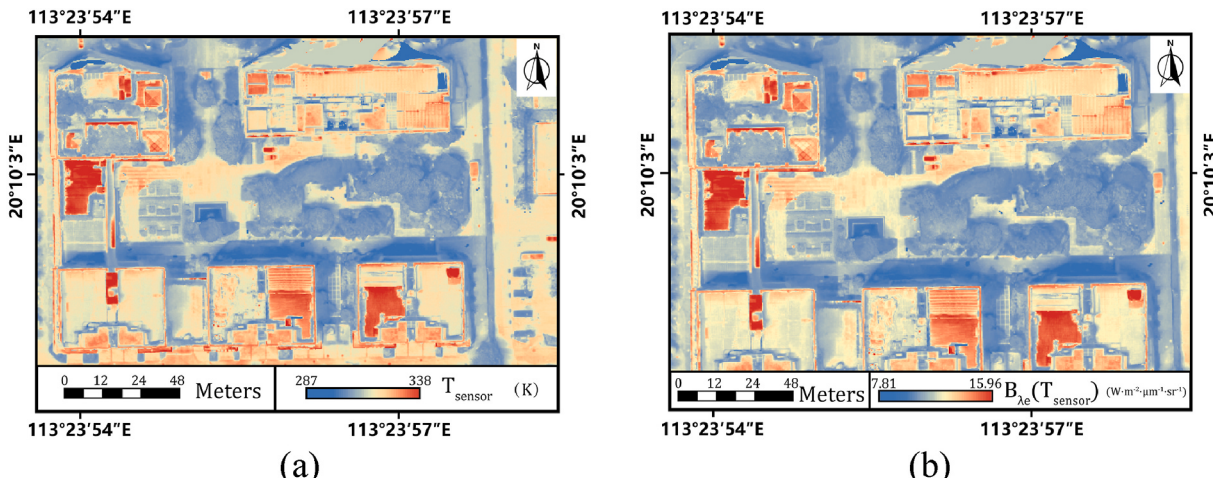


Fig. 7. The retrieved orthophotos of: at-sensor brightness temperature (a) and at-sensor radiance at the effective wavelength (b).

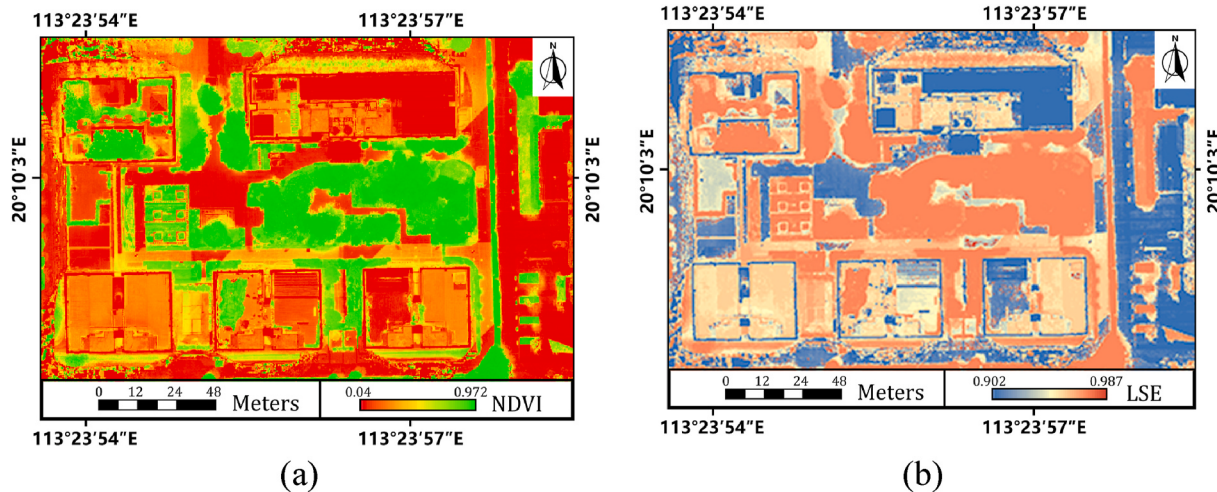


Fig. 8. The retrieved orthophotos of: NDVI (a) and emissivity (b).

$$\text{local} = \min |B'_{\lambda_e}(T_{\text{sensor}}) - B_{\lambda_e}(T_{\text{sensor}})| \quad (12)$$

$$B'_{\lambda_e} = B_i^{\dagger}, \tau_{\lambda_e} = \tau_j, T_{\text{retrieved}} = T_k$$

where  $i, j, k$  are the serial numbers corresponding to the minimum distances, while  $B_i^{\dagger}$ ,  $\tau_j$  and  $T_k$  are the 3DLUT-derived values under such serial numbers.

### 3. Results

#### 3.1. Retrieval of at-sensor brightness temperature and at-sensor radiance

Our statistical results showed that 290 TIR images with 95027200 pixels were collected by FLIR XT2 during the flight. Of these pixels, 99.75% were in the range between 15–65 °C (Fig. 6). Thus, all raw images were converted based on the same palette with this range.

Upon unification of the temperature scale of all the TIR images, the conversion model between the RGB and corresponding  $T_{\text{sensor}}$  was established (Eq. (13)). Based on the statistics, the adjusted coefficient of determination ( $R^2$ ) of this conversion model was 0.986 and the root mean squared error (RMSE) was 0.853K. The metrics of accuracy demonstrated a strong correlation between the two variables, based on which  $T_{\text{sensor}}$  could be accurately converted from the RGB upon unification of the temperature scale.

$$T_{\text{sensor}} = 0.0842 * R + 0.1008 * G + 0.0153 * B + 13.1986 \quad (13)$$

Through the photogrammetry of the processed TIR images and application of the above model, the orthophoto of  $T_{\text{sensor}}$  (Fig. 7a) was generated with a spatial resolution of 87 mm. According to the formula of the effective wavelength (Eq. (2)) and Planck's Equation (Eq. (5)), the pixel-wise at-sensor radiance at the effective wavelength of FLIR XT2 (11.092  $\mu\text{m}$ ) will be retrieved (Fig. 7b) based on the orthophoto of  $T_{\text{sensor}}$ .

The  $T_{\text{sensor}}$  of the whole test area demonstrated a positive relationship with the at-sensor radiance: the  $T_{\text{sensor}}$  ranged from 287 to 338 K, while the radiance received by the sensor fluctuated from 7.81 to 15.96  $\text{W} \cdot \text{m}^{-2} \cdot \mu\text{m}^{-1} \cdot \text{sr}^{-1}$ . Hot spots were concentrated on roofs, as attributed to the properties of the roof materials and the surrounding occlusions. Roofs made of dark plastics had a low specific heat capacity, thus exhibiting strong absorption of visible light. Therefore, more solar radiance was absorbed, and the temperature would rapidly elevate,

thereby emitting more thermal radiance [72,73]. Other roofs made of light-colored metals had a higher shortwave reflectivity than plastic roofs. Thus, such metallic roofs absorbed less solar radiance, thereby emitting less thermal radiation than plastic roofs [74,75]. Lastly, tiles were noted to have a higher specific heat capacity than metallic roofs, which explained the lower thermal radiance emitted by the tiles.

Conversely, cold spots were concentrated on vegetation because of their physiology. Although the shortwave absorption of the vegetation was relatively high, most of the absorbed solar radiation was converted into latent heat through transpiration. At the same time, only a small part was used to heat the vegetation. Thus, the surface temperatures and thermal radiation of the vegetation were lower than those of human-made surfaces.

#### 3.2. Retrieval and validation of pixel-wise LSE

According to Eq. 6, the orthophoto of NDVI was produced after the preprocessing of the multispectral images (Fig. 8a), and the pixel-scale emissivity was calculated according to Eq. 7. To explore the applicability of the emissivity-retrieval model, the absolute differences between the retrieved emissivity and measured emissivity of 8 typical surfaces were examined (Table 1).

The NDVI of almost all vegetations ranged from 0.454 to 0.972, as determined by their growth-related characteristics, such as greenness and density. Comparatively, the NDVI of the human-made surfaces were lower, ranging from 0.004 to 0.454, as determined by the properties of the materials. Furthermore, the results demonstrated that the retrieved emissivity of most vegetations was high and exceeded 0.972, given their higher water content, as paralleled by the literature [56,76]. Conversely, the retrieved emissivity of the human-made surfaces was lower and substantially fluctuated between 0.902 and 0.972.

The measured emissivity of the 8 points was calculated as Eq. (8) based on the ground-measured emissivity spectra. The emissivity of sunlit tiles varied slightly due to the different properties of the measured points. The absolute differences of the sunlit surfaces did not exceed 0.01, which could accordingly be deemed an acceptable value considering some systematic errors in emissivity measurements ( $\pm 0.01$ ). Conversely, the absolute differences of the shaded tiles were more substantial, highlighting the poorer accuracy of the retrieved results for

**Table 1**

Comparison between retrieved emissivity and measured emissivity.

	Sunlit tile1	Sunlit tile2	Sunlit tile3	Sunlit tile4	Sunlit grass1	Sunlit grass2	Shaded tile1	Shaded tile2
Retrieved emissivity	0.937	0.913	0.925	0.936	0.975	0.976	0.974	0.973
Measured emissivity	0.931	0.904	0.918	0.928	0.982	0.984	0.939	0.933
Absolute differences	0.006	0.009	0.007	0.008	0.007	0.008	0.035	0.040

**Table 2**

Accuracy of models characterizing atmospheric parameters at the UAV-height.

	$B_{\lambda_e}^{\uparrow}$	$B_{\lambda_e}^{\downarrow}$	$\tau_{\lambda_e}$
F – statistics	111020.4849	933.5056	91599.1075
R	0.9993	0.9223	0.9991
adjusted –	0.9985	0.8506	0.9982
$R^2$			
RMSE	0.0076	0.3961	0.0008

\* R is the correlation coefficient.

shaded underlying surfaces in this study. Therefore, such findings further suggested that the model would suit urban surfaces with a higher emissivity (exceeding 0.90) under direct sunlight.

### 3.3. Retrieval of pixel-wise atmospheric parameters

The fitting functions of atmospheric upwelling radiance, atmospheric downwelling radiance and transmittance are shown in Eq. (14), and the indicators for evaluating such functions are outlined in Table 2.

$$\begin{aligned} B_{\lambda_e}^{\uparrow} &= 0.0019T_a^2 + 0.0007T_a \cdot RH - 1.1582T_a - 0.2123RH + 173.2867 \\ B_{\lambda_e}^{\downarrow} &= 0.0025T_a^2 + 0.0008RH^2 - 0.0021T_a \cdot RH - 1.1033T_a + 0.5575RH + 110.0847 \\ \tau_{\lambda_e} &= -0.0001T_a^2 - 0.0001T_a \cdot RH + 0.0821T_a + 0.0179RH - 11.2894 \end{aligned} \quad (14)$$

\*Only four decimal places are retained for illustration here in the Equation, while more decimal places are needed for actual calculations.

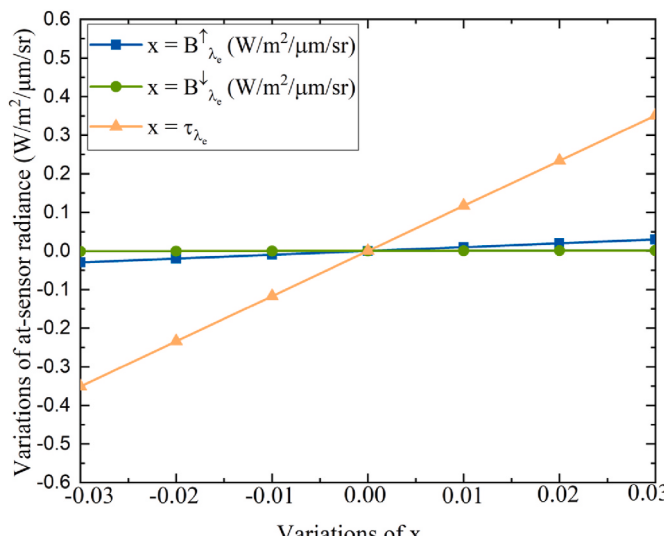


Fig. 9. The sensitivity of at-sensor radiance to three atmospheric parameters ( $B_{\lambda_e}^{\uparrow}$ ,  $B_{\lambda_e}^{\downarrow}$ ,  $\tau_{\lambda_e}$ ).

Our findings (Table 2) provided evidence for the significant correlation between  $B_{\lambda_e}^{\uparrow}$ ,  $B_{\lambda_e}^{\downarrow}$  and  $\tau_{\lambda_e}$ , and the  $T_a$  and  $RH$  near the ground. Thus, the higher predictability of the models further suggested that such models developed by Ref. [47] could be applied not only to naturally open scenes but also to complicated urban scenes with greater spatial heterogeneity.

With the measured ranges of  $T_a$  (300.86–306.16 K) and  $RH$  (31.30–52.07%), the variable ranges of the atmospheric parameters at the height of 100 m were as follows, according to Eq. (14): atmospheric upwelling radiance ( $0.30$ – $0.79 W \cdot m^{-2} \cdot \mu m^{-1} \cdot sr^{-1}$ ); atmospheric downwelling radiance ( $4.24$ – $5.89 W \cdot m^{-2} \cdot \mu m^{-1} \cdot sr^{-1}$ ); atmospheric transmittance ( $0.92$ – $0.96$ ). Based on Eq. (5), the variations of at-sensor radiance caused by changes of three atmospheric parameters ( $\Delta x = 0.01$ ) were respectively shown in Fig. 9.

Each of three low-altitude atmospheric parameters exhibited a positive correlation with the at-sensor radiance: an increment by 0.01 in each of the three parameters caused  $B_{\lambda_e}^{\uparrow}$ ,  $B_{\lambda_e}^{\downarrow}$  and  $\tau_{\lambda_e}$  to respectively increase by about 0.01, 0.0004 and 0.117. Of note, the change of atmospheric downwelling radiance appeared to exert less impact on the at-sensor radiance; it was thus fixed as an average value (5.07) for the subsequent retrieval of the LSTs.

### 3.4. Retrieval and validation of pixel-wise LST

Based on the known pixel-wise emissivity, pixel-wise at-sensor radiance, estimated ranges of atmospheric upwelling radiance plus transmittance and stable atmospheric downwelling radiance, the 3DLUT was established for retrieving the pixel-wise atmospheric upwelling radiance, atmospheric transmittance and LSTs on the whole image. To better account for all situations of the low-altitude atmosphere in the entire test area, the ranges of  $B_i^{\uparrow}$  and  $\tau_j$  were respectively defined as  $0.20$ – $0.89$  and  $0.90$ – $0.98$ ; the step sizes were both set as 0.01. Besides, the range of  $T_k$  was set as  $280$ – $350$ , and its step size was 0.5 given the accuracy of most contact thermometers [77,78] and computational power.

Then, the 3DLUT was employed to calculate the radiance of the whole image, of which each pixel had  $70 \times 9 \times 141$  sets of 3DLUT-referred at-sensor radiance ( $B'_{\lambda_e}(T_{sensor})$ ) (see Fig. 10). For each pixel, the  $B'_{\lambda_e}(T_{sensor})$ ,  $\tau_{\lambda_e}$  and  $T_{retrieved}$  were determined by the minimum distance between  $B'_{\lambda_e}(T_{sensor})$  and  $B_{\lambda_e}(T_{sensor})$ . Therefore, the orthophotos of the atmospheric upwelling radiance, atmospheric transmittance and retrieved temperatures were derived (Fig. 11).

An evident finding was that the retrieved atmospheric upwelling radiance and atmospheric transmittance were changeable pixel by pixel:  $B_{\lambda_e}^{\uparrow}$  ranged from  $0.30$  to  $0.79 W \cdot m^{-2} \cdot \mu m^{-1} \cdot sr^{-1}$ , while  $\tau_{\lambda_e}$  ranged from  $0.92$  to  $0.95 W \cdot m^{-2} \cdot \mu m^{-1} \cdot sr^{-1}$ . Additionally, the distribution of  $T_{retrieved}$  resembled that of  $T_{sensor}$ , ranging from  $293$  to  $343$  K. Nonetheless,  $T_{retrieved}$  was higher than  $T_{sensor}$ , especially for rooftops and hard

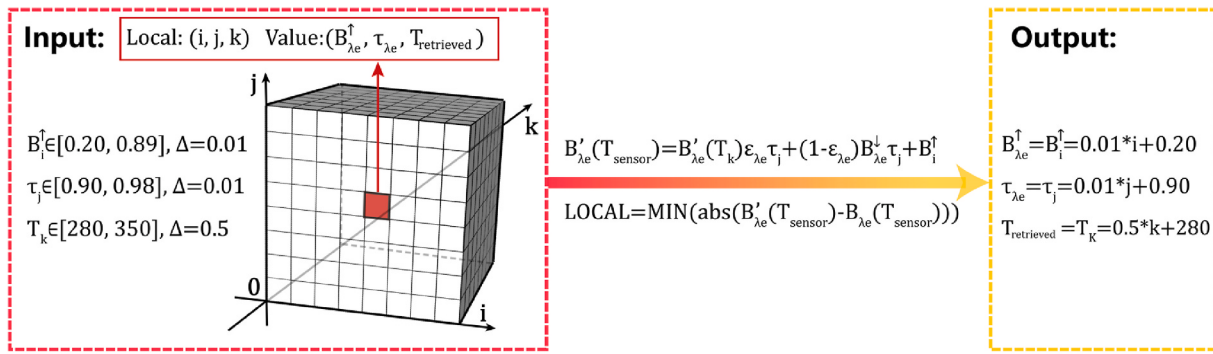


Fig. 10. The 3DLUT of the whole image established by  $B_{\lambda_e}^dagger$ ,  $\tau_{\lambda_e}$  and  $T_{\text{retrieved}}$ .

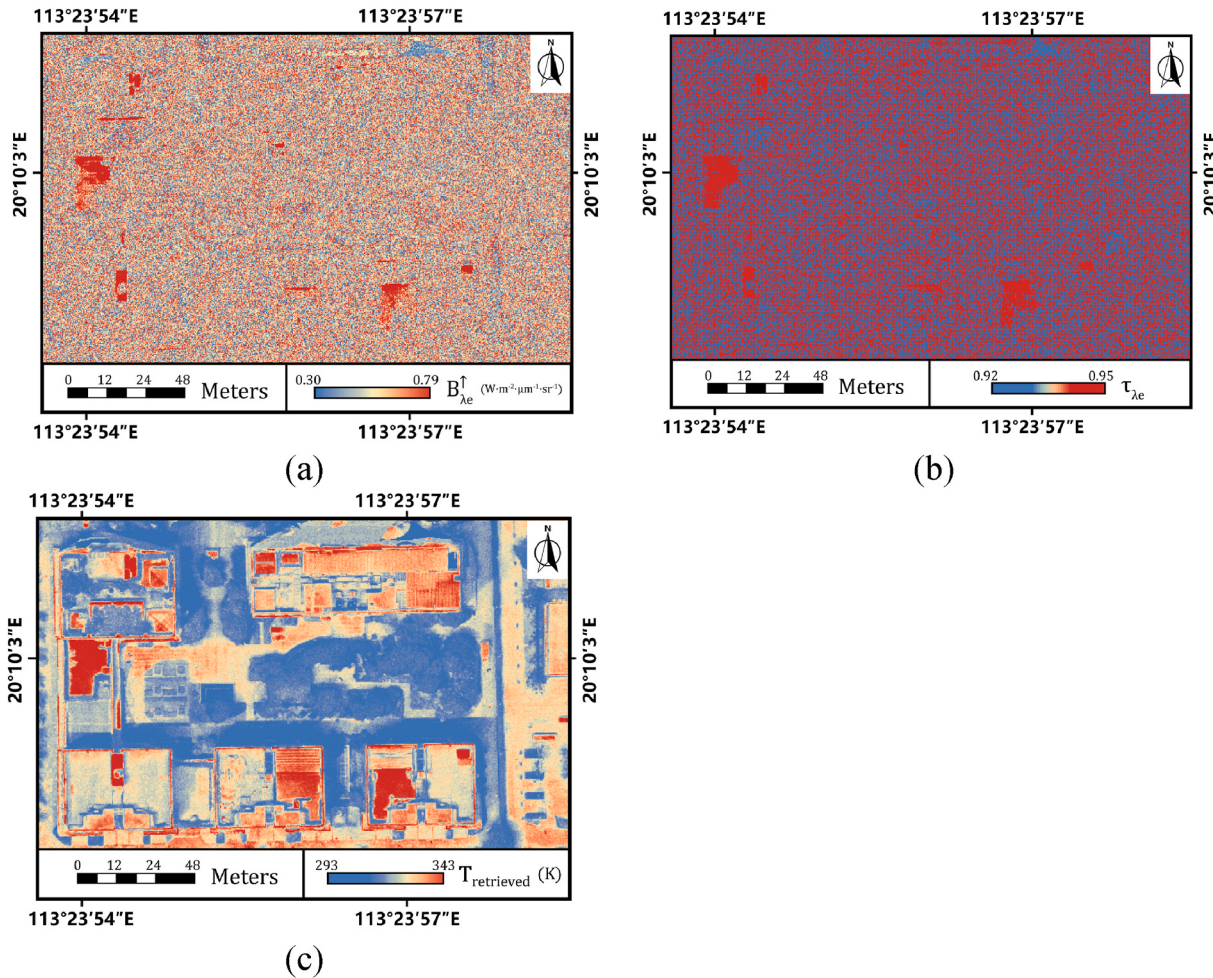


Fig. 11. The retrieved orthophotos of:  $B_{\lambda_e}^dagger$  (a),  $\tau_{\lambda_e}$  (b) and  $T_{\text{retrieved}}$  (c).

underlying surfaces. This could be attributed to the measurement of  $T_{\text{sensor}}$  by a thermal imager without factoring in corrections of emissivity. Finally,  $T_{\text{retrieved}}$  was validated with the  $T_{\text{measured}}$  of 16 points, and the  $T_{\text{retrieved}}$  of 16 points were also compared with temperature readings ( $T_{\text{read}}$ ) of the corresponding single frame via the FLIR Tools software (Fig. 12).

Analysis of the absolute differences demonstrated the superiority of  $T_{\text{retrieved}}$  for characterizing the distribution of LSTs, all of which were less than 2.6 K for heterogeneous underlying surfaces under different lighting conditions. Among these, the absolute differences of most sunlit underlying surfaces were less than 1.5 K, while those of shaded ones

were as high as 2.6 K due to errors in retrieved emissivity. By contrast, larger differences up to 4.7 K were noted between the actual LSTs and corresponding temperature readings from the FLIR Tools software. The reason was that the RTE of the software differed from that in this paper, which warranted more parameters that were challenging to access; these parameters were generally defaulted and inaccurate and thus led to large errors in temperatures [79].

To examine the  $T_{\text{retrieved}}$  of each type of surface, a deep-learning method was employed to classify the processed multispectral images via the hybridSN algorithm of Python and IDL languages [80]. Eight types of representative surfaces were selected, from which training and

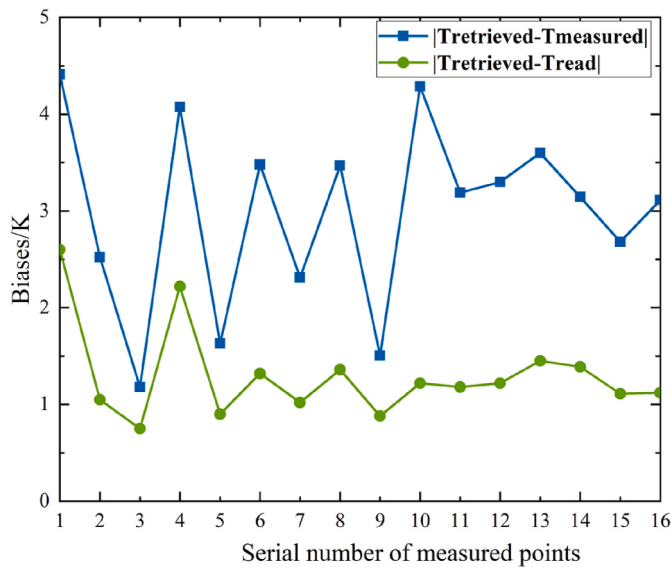


Fig. 12. Comparisons between  $T_{\text{retrieved}}$  and  $T_{\text{measured}}$  plus  $T_{\text{retrieved}}$  and  $T_{\text{read}}$ .

testing samples were chosen via the ENVI software. The results (Fig. 13a) demonstrated that most surfaces were assigned to the correct categories with an overall accuracy of 97.65%. Sunlit vegetation and sunlit tiles registered higher accuracy than other surfaces, whereas some shaded natural surfaces were misclassified as shaded tiles or water because of their similar spectral characteristics. Rooftop surfaces were classified into higher- and lower-emissivity materials. Given the large and varied sample size, such rooftop surfaces registered reasonably good accuracy.

Upon geographically registering the classification results with LST-retrieval mapping (Fig. 11c), the average  $T_{\text{retrieved}}$  of each classified surface was computed: grass (314.93 K); shrub (313.08 K); tree (308.70 K); sunlit tile (320.60 K); shaded tile (309.74 K); rooftop1 (319.56 K); rooftop2 (323.25 K); and water (312.66 K). Natural surfaces (i.e. vegetation and water) registered lower  $T_{\text{retrieved}}$  than most human-made surfaces because of their physiological characteristics. Additionally, shaded tiles registered the lowest average  $T_{\text{retrieved}}$ , suggesting that the shading of buildings critically reduced the temperatures of underlying surfaces.

Conversely, Rooftop2 (composed of lower-emissivity materials) registered the highest average  $T_{\text{retrieved}}$ , given the lower specific heat capacity and substantial absorption of visible light and solar radiation [81]. This was followed by sunlit tiles and rooftop1 because they were composed of materials with a higher specific heat capacity [72]. Furthermore, the range of  $T_{\text{retrieved}}$  of trees was narrower than those of grasses and shrubs (Fig. 13b), as attributed to the uniformity of foliage of the trees. By contrast, the  $T_{\text{retrieved}}$  of almost all the human-made surfaces were more spread out and fluctuated substantially, given their heterogeneous compositions. Lastly, while some abnormal points were observed, they were negligible since each point denoted only one pixel.

#### 4. Discussion

##### 4.1. Approach for obtaining at-sensor radiance from the UAV-derived TIR images with the R-JPEG format

An approach was proposed in this paper through the secondary development of the FLIR data (Section 2.4.1). This approach addressed the drawback that almost all UAV-derived TIR images lack accurate calibration parameters outdoors, and it is thus impossible to obtain accurate at-sensor radiance outdoors, especially for TIR images with the R-JPEG format. Based on the colored images upon unification of the temperature scale, the quality of the reconstructed orthophoto of  $T_{\text{sensor}}$

could be improved; besides, abnormal temperatures caused by the temperature drift of the thermal imager [31,32,35] could be eliminated and thereby the thermal resolution would be enhanced. Hence, this method could consistently and accurately provide the at-sensor brightness temperatures, thereby ensuring a reliable methodological basis for determining the precise at-sensor radiance for an improved regional analysis of an outdoor thermal environment.

##### 4.2. Sensitivity analysis of retrieved LSTs

To retrieve accurate LSTs, aspects such as emissivity, wavelength, at-sensor brightness temperature and atmospheric parameters would be required (Eq. (3)). However, such inputs introduced uncertainties in the retrieved temperature, and thus the following formula was employed:

$$\Delta T_{\text{retrieved}} = |T_{\text{retrieved}}(x + \Delta x) - T_{\text{retrieved}}(x)| \quad (15)$$

where  $\Delta T_{\text{retrieved}}$  is the error of the retrieved temperature,  $x$  is the input for analyzing the sensitivity of  $T_{\text{retrieved}}$ , and  $\Delta x$  is the uncertainty of this input.  $T_{\text{retrieved}}(x)$  and  $T_{\text{retrieved}}(x + \Delta x)$  respectively denote retrieved temperatures for  $x$  and  $x + \Delta x$ .

To perform the sensitivity analysis, the method of control variable was used. Based on Eq. (3), the average values of most inputs were taken as the reference values:  $\varepsilon_{\lambda_e}$  (0.96);  $\lambda_e$  (11.092);  $T_{\text{sensor}}$  (313.63);  $B_{\lambda_e}^{\dagger}$  (0.55);  $B_{\lambda_e}^{\perp}$  (5.07); and  $\tau_{\lambda_e}$  (0.94). Errors in the temperature-retrieval caused by deviations of wavelength and at-sensor brightness temperature ( $\Delta x = 0.5$ ) are outlined in Fig. 14.a, while those caused by uncertainties of other inputs ( $\Delta x = 0.01$ ) are outlined in Fig. 14.b.

Except for at-sensor brightness temperature, other parameters negatively correlate with the retrieved temperature. Sensitive analysis demonstrated the critical roles of at-sensor brightness temperature, atmospheric transmittance and LSE in affecting retrieved temperatures: an uncertainty of 0.5 K in  $T_{\text{sensor}}$  led to an absolute error of around 0.54 K in  $T_{\text{retrieved}}$  while a 1% deviation in  $\tau_{\lambda_e}$  and  $\varepsilon_{\lambda_e}$  led to absolute errors of about 0.81 and 0.51 K in  $T_{\text{retrieved}}$ . Conversely, the accuracy of  $T_{\text{retrieved}}$  was only moderately governed by wavelength, atmospheric upwelling and downwelling radiances: errors of 0.5 for these parameters led respectively to absolute errors of approximately 0.02 K, 0.07 K and 0.003 K in  $T_{\text{retrieved}}$ . Such observations offered numerous insights. Firstly, the  $T_{\text{retrieved}}$  exhibited the highest sensitivity to the  $\tau_{\lambda_e}$ ; this further demonstrated the necessity to retrieve the pixel-wise atmospheric transmittance, which was crucially influenced by  $T_a$  and  $RH$ , especially under unstable weathers. Secondly, the  $T_{\text{retrieved}}$  exhibited a similarly high sensitivity to  $T_{\text{sensor}}$  and  $\varepsilon_{\lambda_e}$ : the accuracy of  $T_{\text{sensor}}$  was, in turn, critically governed by the internal temperature of the thermal imager [33]. To stabilize the internal temperature of the sensor, it would be crucial to warm up the uncooled thermal cameras before data acquisition. Additionally, the accuracy of  $\varepsilon_{\lambda_e}$  was determined by the characteristics of materials [56] and varied on the pixel scale. It would thus not be judicious to replace the pixel-level varied emissivity of urban surfaces with a fixed value of a certain type of surface. Instead, the models of emissivity-retrieval for urban surfaces should be improved, especially for surfaces under different lighting conditions. Thirdly, although the  $T_{\text{retrieved}}$  showed less correlation with the  $B_{\lambda_e}^{\dagger}$ , the spatial variations of  $B_{\lambda_e}^{\dagger}$  (0.30–0.79  $W \cdot m^{-2} \cdot \mu m^{-1} \cdot sr^{-1}$ ) would lead to the changes of  $T_{\text{retrieved}}$  up to 3.46 K. Therefore, it is also essential to retrieve the pixel-wise atmospheric upwelling radiance. Lastly, the  $T_{\text{retrieved}}$  was not influenced by the  $\lambda_e$  if the error of  $\lambda_e$  was less than 1  $\mu m$ . Besides, the spatial variations of  $B_{\lambda_e}^{\perp}$  (4.24–5.89  $W \cdot m^{-2} \cdot \mu m^{-1} \cdot sr^{-1}$ ) also exerted little effect on  $T_{\text{retrieved}}$  ( $\Delta T_{\text{retrieved}} = 0.42$  K). This further justified fixing the atmospheric downwelling radiance during the LST-retrieval process; the  $B_{\lambda_e}^{\perp}$  accounted for a smaller proportion of at-sensor radiance because most surfaces had higher emissivity and thus reflected less downwelling radiance to the sensor.

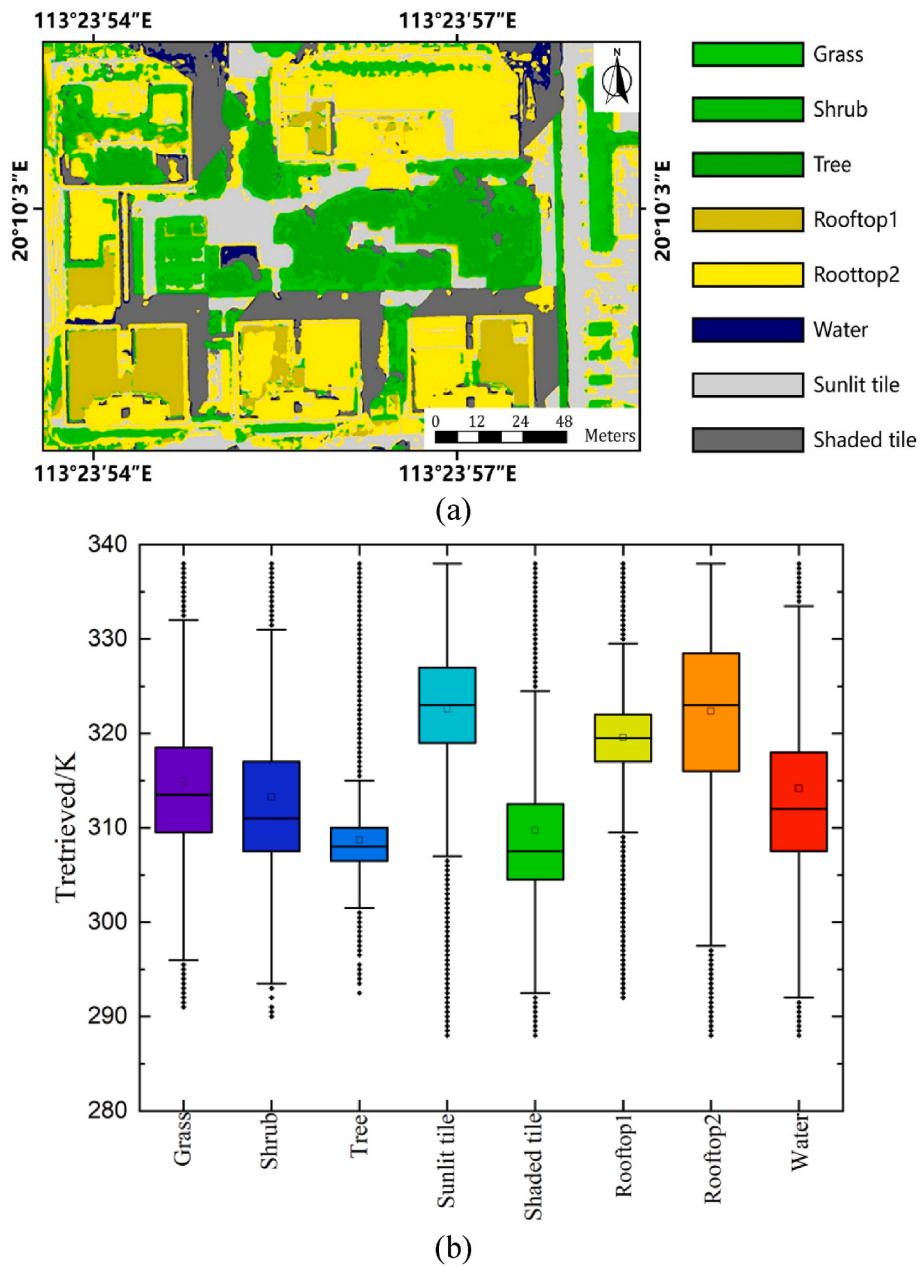


**Fig. 13.** (a) Classified mapping based on processed multispectral images, and (b)  $T_{retrieved}$  of eight typical surfaces.

\* Rooftop1 refers to materials with a higher emissivity, while Rooftop2 refers to materials with a lower emissivity.

#### 4.3. Advantages and disadvantages of TRUB-3DLUT

It is noteworthy in LST retrieval that empirical models [31,33,35,36], which are both labor- and resource-intensive, have not been commonly employed. Through analysis of the process of radiative transfer and measured data, this study proposed a method that could be applied to other times, given appropriate adjustments in the ranges of the corresponding parameters in the look-up table. Although some studies have suggested LST-retrieval from UAV-derived images based on the RTE [47,82,83], their estimated pixelwise LSE typically originated from employing LSE-retrieval model derived from satellite data. It should be recognized that differences in the spatial resolution would introduce retrieved errors of LSE and compromise the retrieved accuracy of LSTs, especially for urban underlying surfaces with high heterogeneity. Besides, pixelwise atmospheric parameters have been either omitted in such studies or assumed to be uniform above the larger area,

further compromising the micro-scale accuracy. This study comprehensively considered factors affecting the retrieved temperatures and analyzed the sensitivity of UAV-derived temperatures. Our results obtained by the TRUB-3DLUT methodology have not only offset the lack of LSE and atmospheric parameters with high accuracy and spatial resolution, but also provided more accurate LSTs than those in previous studies for which the retrieved errors were reported to exceed almost 3 K during aerial operations [28,30,33].

Several disadvantages of the TRUB-3DLUT are noteworthy. Firstly, although it considered thermal radiance emitted by the urban pixel, downward radiance reflected by the urban pixel, and upward radiance emitted by the low-altitude atmosphere, it did not account for surrounding radiance scattered by the adjacent pixels [84]. The lack of consideration of the effects of geometry and adjacency on LST-retrieval from the TIR images with high spatial resolution might compromise the accuracy of the retrieved LSTs, especially for buildings with a lower sky

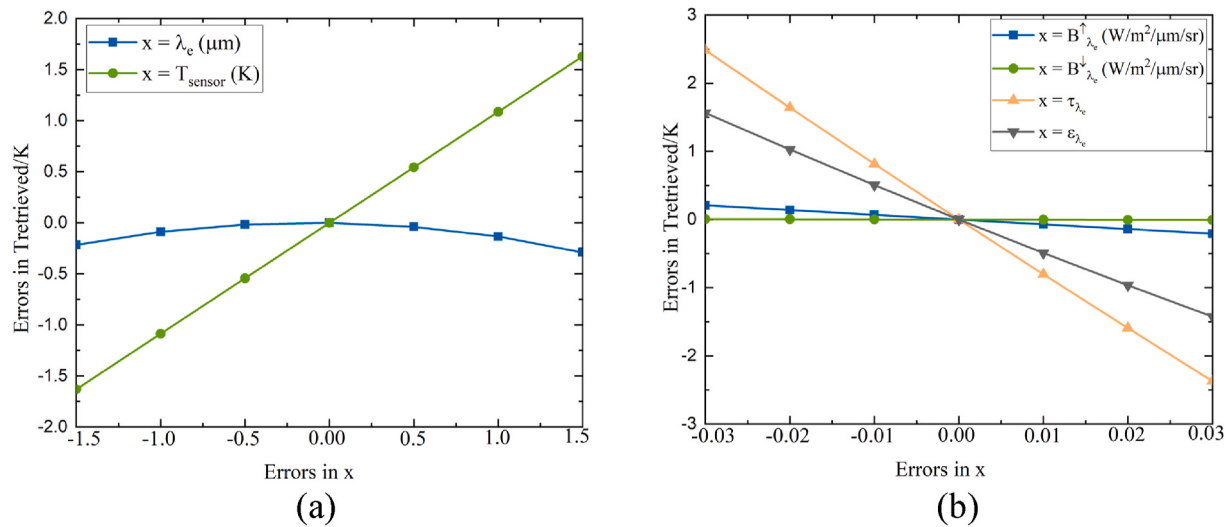


Fig. 14. Errors in retrieved temperatures caused by (a) errors due to LSE and (b) errors due to other parameters.

view factor [51,85]. Accordingly, future research should focus on improving the RTE while considering multiple scattering from the adjacent pixels. Secondly, the  $T_{\text{retrieved}}$  of rooftops with a lower emissivity was probably underestimated, given the retrieved errors of emissivity. Such rooftops were composed of lower-emissivity materials (e.g. metals and plastic) [86,87], while lower-emissivity surfaces were excluded from this retrieval model [63]. This might account for more substantial retrieved errors of the roofs in this study. Additionally, the  $T_{\text{retrieved}}$  of shaded tiles tended to register larger differences with the  $T_{\text{measured}}$ . This was because the retrieved model (Eq. 7) had been established under the direct sunlight, which ignored differences between the spectra of the sunlit and shaded surfaces. Given the higher sensitivity of  $T_{\text{retrieved}}$  to LSE, it would be crucial to more accurately retrieve LSE. Hence, emissivity should ideally be retrieved under sunlit conditions and the spectra of more urban surfaces should be collected to improve the generalizability of the emissivity-retrieval model. Lastly, to obtain more accurate LSTs with a high spatiotemporal resolution and to analyze daily variations of surface urban heat islands, the TRUB-3DLUT could be combined with models of diurnal temperature cycle, since UAVs equipped with thermal images could enable frequent and real-time observations [14,88,89].

## 5. Conclusion

This paper has proposed a methodology involving a 3DLUT to characterize parameters that would be challenging to obtain for complex RTE, thereby improving the accuracy of retrieved LSTs under the influences of uncertainties of various inputs. Numerous conclusions were drawn, as follows:

- 1) The process of converting RGB into at-sensor brightness temperature in batches achieved a high theoretical accuracy (*adjusted – R*<sup>2</sup>: 0.986; *RMSE*: 0.853 K).
- 2) The emissivity-retrieval model performed optimally for sunlit surfaces with a higher emissivity (above 0.90), with an absolute bias less than 0.01.
- 3) The retrieved LSTs were aligned with the *in-situ* LSTs, and the errors of sunlit surfaces with a higher emissivity were less than 1.5 K.
- 4) The retrieved LSTs were more critically affected by the LSE and atmospheric transmittance but were less so by the wavelength and atmospheric downwelling radiance.

The findings have collectively demonstrated the promising accuracy of the TRUB-3DLUT in the LST-retrieval of urban underlying surfaces, offering practical utility in applications such as larger-scale monitoring of surface heat urban islands and rapid micro-scale evaluation of thermal environments.

## CRediT authorship contribution statement

**Xue Zhong:** Writing – review & editing, Writing – original draft, Validation, Software, Methodology, Investigation, Formal analysis, Data curation, Conceptualization. **Lihua Zhao:** Supervision, Project administration, Funding acquisition, Conceptualization. **Jie Wang:** Software, Methodology, Data curation. **Xiang Zhang:** Visualization, Investigation. **Zichuan Nie:** Visualization. **Yingtan Li:** Software, Methodology, Data curation. **Peng Ren:** Supervision, Resources, Project administration, Funding acquisition, Data curation, Conceptualization.

## Declaration of competing interest

The authors declare that they have no known competing financial interests or personal relationships that could have appeared to influence the work reported in this paper.

## Data availability

Data will be made available on request.

## Acknowledgments

This project has been supported by National Key R&D Program of China (No. 2019YFE0124500), National Natural Science Foundation of China (No. 52278108, 51878288), Natural Science Foundation of Guangdong (No. 2021A1515011059, 2019A1515010705), the Fundamental Research Funds for the Central Universities of China (No. 2020ZYGXZR090), and Innovation Team Project of China West Normal University (CXTD2020-3). Additionally, we are thankful for the assistance provided by the PhD Ziwei Wang (a member of Prof. Ji Zhou's team) from the School of Resources and Environment, University of Electronic Science and Technology of China.

## Appendix A

The technical parameters of sensors on the UAV are displayed in Table A.1, and the parameters of other equipment are shown in Table A.2 and Table A.3.

**Table A.1**

The technical parameters of sensors on the UAV

Notation	Description	
	Micasense RedEdge-MX Nano-Hyperspec imager	FLIR XT2
Size	8.7 cm × 5.9 cm × 4.54 cm	11.80 cm × 11.16 cm × 12.55 cm
Weight	231.9 g	588 g
Resolution	1280 × 960	640 × 512
Temperature range	0–50 °C	–25 – 135 °C
Spectral range	400–900 nm	7.5–13.5 μm
Spectral bands	Blue, green, red, red edge, near-infrared	Thermal infrared
Field of view	47.2 ° (HFOV)	32 × 26 ° (FOV)
Output Type	TIFF	R-JPEG/JPEG/TIFF

**Table A.2**

The technical parameters of 102F portable Fourier transform thermal infrared spectrometer

Indicator	Specific Parameters
Size	36 cm × 20 cm × 23 cm
Spectral range	2–16 μm
Spectral resolution	4, 8, 16 cm <sup>-1</sup> (Adjustable)
Spectral accuracy	±1 cm <sup>-1</sup> (Entire spectral range)
The proper working temperature range	15–35 K
The method of exporting data	Via USB

**Table A.3**

The parameters of other equipment

Parameters	Equipment	Range	Accuracy
Shortwave/Longwave radiation	Pyranometer: KIPPZONE CMP3 Pyrgeometer: KIPPZONE CGR 3	Pyranometer: 0–2000 W/m <sup>2</sup> (300–2800 nm) Pyrgeometer: 250–250 W/m <sup>2</sup> (4.5–42 μm)	Pyranometer: < 4 % (–10–40 °C) Pyrgeometer: < 5 % (–10–40 °C)
Ground temperature	HOBO TMC6-HE	40–100 °C	±0.21 °C
Air temperature	HOBO MX2302A	–40–70 °C	±0.2 °C (0–70 °C)
Relative humidity	HOBO MX2302A	0–100%	±2.5% (10–90%)
Wind speed	Delta AP3203.2	0.1–5 m/s	±0.05 m/s
Globe temperature	Delta TP3276.2	–10–100 °C	±0.1 °C

## References

- [1] A. Siddiqui, G. Kushwaha, B. Nikam, S.K. Srivastav, A. Shelar, P. Kumar, Analysing the day/night seasonal and annual changes and trends in land surface temperature and surface urban heat island intensity (SUHII) for Indian cities, *Sustain. Cities Soc.* 75 (2021), 103374.
- [2] A. Mathew, S. Khandelwal, N. Kaul, S. Chauhan, Analyzing the diurnal variations of land surface temperatures for surface urban heat island studies: is time of observation of remote sensing data important? *Sustain. Cities Soc.* 40 (2018) 194–213.
- [3] M.F.U. Moazzam, Y.H. Doh, B.G. Lee, Impact of urbanization on land surface temperature and surface urban heat Island using optical remote sensing data: a case study of Jeju Island, Republic of Korea, *Build. Environ.* 222 (2022), 109368.
- [4] M. Nunez, T.R. Oke, The energy balance of an urban canyon, *J. Appl. Meteorol.* 16 (1) (1977) 11–19.
- [5] N.G. Machado, M.S. Biudes, L.P. Angelini, C.A.S. Querino, P.C.B. da Silva Angelini, Impact of changes in surface cover on energy balance in a tropical city by remote sensing: a study case in Brazil, *Remote Sens. Appl.: Soc. Environ.* 20 (2020), 100373.
- [6] J. Park, S.-O. Hwang, Impacts of spectral nudging on the simulated surface air temperature in summer compared with the selection of shortwave radiation and land surface model physics parameterization in a high-resolution regional atmospheric model, *J. Atmos. Sol. Terr. Phys.* 164 (2017) 259–267.
- [7] P.K. Cheung, C.Y. Jim, P.L. Hung, Preliminary study on the temperature relationship at remotely-sensed tree canopy and below-canopy air and ground surface, *Build. Environ.* 204 (2021), 108169.
- [8] J. Xue, M.C. Anderson, F. Gao, C. Hain, L. Sun, Y. Yang, K.R. Knipper, W.P. Kustas, A. Torres-Rua, M. Schull, Sharpening ECOSTRESS and VIIRS land surface temperature using harmonized Landsat-Sentinel surface reflectances, *Rem. Sens. Environ.* 251 (2020), 112055.
- [9] T.H.G. Vidal, P. Gamet, A. Olioso, F. Jacob, Optimizing TRISHNA TIR channels configuration for improved land surface temperature and emissivity measurements, *Rem. Sens. Environ.* 272 (2022), 112939.
- [10] P. Hesslerová, J. Pokorný, J. Brom, A. Rejková – Procházková, Daily dynamics of radiation surface temperature of different land cover types in a temperate cultural landscape: consequences for the local climate, *Ecol. Eng.* 54 (2013) 145–154.
- [11] Y. Zhang, L. Sun, Spatial-temporal impacts of urban land use land cover on land surface temperature: case studies of two Canadian urban areas, *Int. J. Appl. Earth Obs. Geoinf.* 75 (2019) 171–181.
- [12] X. Chen, Y. Zhang, Impacts of urban surface characteristics on spatiotemporal pattern of land surface temperature in Kunming of China, *Sustain. Cities Soc.* 32 (2017) 87–99.
- [13] S. Ghosh, D. Kumar, R. Kumari, Assessing Spatiotemporal Dynamics of Land Surface Temperature and Satellite-Derived Indices for New Town Development and Suburbanization Planning, *Urban Governance*, 2022.
- [14] P. Dong, S. Jiang, W. Zhan, C. Wang, S. Miao, H. Du, J. Li, S. Wang, L. Jiang, Diurnally continuous dynamics of surface urban heat island intensities of local

- climate zones with spatiotemporally enhanced satellite-derived land surface temperatures, *Build. Environ.* 218 (2022), 109105.
- [15] M. Lemos-Canovas, J. Martin-Vide, M.C. Moreno-Garcia, J.A. Lopez-Bustins, Estimating Barcelona's metropolitan daytime hot and cold poles using Landsat-8 Land Surface Temperature, *Sci. Total Environ.* 699 (2020), 134307.
- [16] Z.-L. Li, B.-H. Tang, H. Wu, H. Ren, G. Yan, Z. Wan, I.F. Trigo, J.A. Sobrino, Satellite-derived land surface temperature: current status and perspectives, *Remote Sens. Environ.* 131 (2013) 14–37.
- [17] H. Wang, K. Mao, Z. Yuan, J. Shi, M. Cao, Z. Qin, S. Duan, B. Tang, A method for land surface temperature retrieval based on model-data-knowledge-driven and deep learning, *Rem. Sens. Environ.* 265 (2021), 112665.
- [18] X. Ye, H. Ren, Y. Liang, J. Zhu, J. Guo, J. Nie, H. Zeng, Y. Zhao, Y. Qian, Cross-calibration of Chinese Gaofen-5 thermal infrared images and its improvement on land surface temperature retrieval, *Int. J. Appl. Earth Obs. Geoinf.* 101 (2021), 102357.
- [19] T. Hu, H. Li, B. Cao, A.I.J.M. van Dijk, L.J. Renzullo, Z. Xu, J. Zhou, Y. Du, Q. Liu, Influence of emissivity angular variation on land surface temperature retrieved using the generalized split-window algorithm, *Int. J. Appl. Earth Obs. Geoinf.* 82 (2019), 101917.
- [20] C. Yoo, J. Im, D. Cho, Y. Lee, D. Bae, P. Sismanidis, Downscaling MODIS nighttime land surface temperatures in urban areas using ASTER thermal data through local linear forest, *Int. J. Appl. Earth Obs. Geoinf.* 110 (2022), 102827.
- [21] Q. Weng, P. Fu, F. Gao, Generating daily land surface temperature at Landsat resolution by fusing Landsat and MODIS data, *Rem. Sens. Environ.* 145 (2014) 55–67.
- [22] J. Cheng, X. Meng, S. Dong, S. Liang, Generating the 30-m land surface temperature product over continental China and USA from landsat 5/7/8 data, *Sci. Rem. Sens.* 4 (2021), 100032.
- [23] W.A. Heckley, J.-J. Morcrette, E. Klinker, Applications of satellite radiance data in the medium range forecasting environment at ECMWF, *Adv. Space Res.* 12 (7) (1992) 303–312.
- [24] P. Dash, A. Ignatov, Validation of clear-sky radiances over oceans simulated with MODTRAN4.2 and global NCEP GDAS fields against nighttime NOAA15-18 and MetOp-A AVHRR data, *Rem. Sens. Environ.* 112 (6) (2008) 3012–3029.
- [25] W. Tang, J. Qin, K. Yang, F. Zhu, X. Zhou, Does ERA5 outperform satellite products in estimating atmospheric downward longwave radiation at the surface? *Atmos. Res.* 252 (2021), 105453.
- [26] M. Si, B.H. Tang, Z.L. Li, Estimation of land surface temperature from unmanned aerial vehicle loaded thermal imager data, in: IGARSS 2018 - 2018 IEEE International Geoscience and Remote Sensing Symposium, 2018.
- [27] P. Smith, P. Sarricolea, O. Peralta, J.P. Aguilera, F. Thomas, Study of the urban microclimate using thermal UAV. The case of the mid-sized cities of Arica (arid) and Curicó (Mediterranean), Chile, *Build. Environ.* 206 (2021).
- [28] B. Song, K. Park, Verification of accuracy of unmanned aerial vehicle (UAV) land surface temperature images using in-situ data, *Rem. Sens.* 12 (2) (2020).
- [29] Y. Malbeteau, S. Parkes, B. Aragon, J. Rosas, M.F. McCabe, Capturing the diurnal cycle of land surface temperature using an unmanned aerial vehicle, *Rem. Sens.* 10 (9) (2018).
- [30] D. Kim, J. Yu, J. Yoon, S. Jeon, S. Son, Comparison of accuracy of surface temperature images from unmanned aerial vehicle and satellite for precise thermal environment monitoring of urban parks using in situ data, *Rem. Sens.* 13 (10) (2021).
- [31] F.-J. Mesas-Carrascosa, F. Pérez-Porras, J. Meroño de Larriva, C. Mena Frau, F. Agüera-Vega, F. Carvajal-Ramírez, P. Martínez-Carricondo, A. García-Ferrer, Drift correction of lightweight microbolometer thermal sensors on-board unmanned aerial vehicles, *Rem. Sens.* 10 (4) (2018).
- [32] R. Olbricht, B. Wiecek, G. De Mey, Thermal drift compensation method for microbolometer thermal cameras, *Appl. Opt.* 51 (2012) 1788–1794.
- [33] M.G. Acorsi, L.M. Giménez, M. Martello, Assessing the performance of a low-cost thermal camera in proximal and aerial conditions, *Rem. Sens.* 12 (21) (2020).
- [34] X. Zhong, L. Zhao, H. Zheng, Y. Li, Y. Zhang, P. Ren, An improved model for emissivity retrieval of complex urban surfaces based on spectral indices from UAV, *Sustain. Cities Soc.* 84 (2022), 104032.
- [35] J. Kelly, N. Kljun, P.-O. Olsson, L. Mihai, B. Liljeblad, P. Weslien, L. Klemedtsson, L. Eklundh, Challenges and best practices for deriving temperature data from an uncalibrated UAV thermal infrared camera, *Rem. Sens.* 11 (5) (2019) 567–588.
- [36] Q. Wan, B. Brede, M. Smigaj, L. Kooistra, Factors influencing temperature measurements from miniaturized thermal infrared (TIR) cameras: a laboratory-based approach, *Sensors* 21 (24) (2021).
- [37] F. Chen, S. Yang, Z. Su, K. Wang, Effect of emissivity uncertainty on surface temperature retrieval over urban areas: investigations based on spectral libraries, *ISPRS J. Photogramm.* 114 (2016) 53–65.
- [38] H. Ren, R. Liu, Q. Qin, W. Fan, L. Yu, C. Du, Mapping finer-resolution land surface emissivity using Landsat images in China, *JGR: Atmospheres* 122 (13) (2017) 6764–6781.
- [39] G.C. Hulley, S.J. Hook, E. Abbott, N. Malakar, T. Islam, M. Abrams, The ASTER global emissivity dataset (ASTER GED): mapping earth's emissivity at 100 meter spatial scale, *Geophys. Res. Lett.* 42 (19) (2015) 7966–7976.
- [40] H. Li, R.B. Li, Y.K. Yang, B. Cao, Z.J. Bian, T. Hu, Y.M. Du, L. Sun, Q.H. Liu, Temperature-based and radiance-based validation of the collection 6 MYD11 and MYD21 land surface temperature products over barren surfaces in northwestern China, *IEEE Trans. Geosci. Rem. Sens.* 59 (2) (2021) 1794–1807.
- [41] A. Sekertekin, S. Bonafoni, Land surface temperature retrieval from landsat 5, 7, and 8 over rural areas: assessment of different retrieval algorithms and emissivity models and toolbox implementation, *Rem. Sens.* 12 (2) (2020).
- [42] J.C. Jimenez-Munoz, J.A. Sobrino, D. Skokovic, C. Mattar, J. Cristobal, Land surface temperature retrieval methods from landsat-8 thermal infrared sensor data, *Geosci. Rem. Sens. Lett.* IEEE 11 (10) (2014) 1840–1843.
- [43] D.B. Ji, J.C. Shi, T.X. Wang, C. Xiong, Q. Cui, Ieee, ATMOSPHERE EFFECT ANALYSIS and ATMOSPHERE CORRECTION of AMSR-E BRIGHTNESS TEMPERATURE over LAND, 2014 IEEE INTERNATIONAL GEOSCIENCE and REMOTE SENSING SYMPOSIUM, IGARSS, 2014, pp. 4107–4110.
- [44] Z.L. Liu, H. Wu, B.H. Tang, S. Qiu, Z.L. Li, Atmospheric corrections of passive microwave data for estimating land surface temperature, *Opt Express* 21 (13) (2013) 15654–15663.
- [45] M.M. Wang, G.J. He, Z.M. Zhang, G.Z. Wang, Z.H. Wang, R.Y. Yin, S.A. Cui, Z. J. Wu, X.J. Cao, A radiance-based split-window algorithm for land surface temperature retrieval: theory and application to MODIS data, *Int. J. Appl. Earth Obs. Geoinf.* 76 (2019) 204–217.
- [46] J.C. Jiménez-Muñoz, J.A. Sobrino, A generalized single-channel method for retrieving land surface temperature from remote sensing data, *JGR: Atmospheres* 108 (D22) (2003).
- [47] Z. Wang, J. Zhou, S. Liu, M. Li, X. Zhang, Z. Huang, W. Dong, J. Ma, L. Ai, A land surface temperature retrieval method for UAV broadband thermal imager data, *Geosci. Rem. Sens. Lett.* IEEE 19 (2022) 1–5.
- [48] H.L. Shao, C.Y. Liu, C.L. Li, J.Y. Wang, F. Xie, Temperature and emissivity inversion accuracy of spectral parameter changes and noise of hyperspectral thermal infrared imaging spectrometers, *Sensors* 20 (7) (2020).
- [49] W. Yang, B. Matsushita, J. Chen, T. Fukushima, Estimating constituent concentrations in case II waters from MERIS satellite data by semi-analytical model optimizing and look-up tables, *Rem. Sens. Environ.* 115 (5) (2011) 1247–1259.
- [50] L. Li, X. Xin, H. Zhang, J. Yu, Q. Liu, S. Yu, J. Wen, A method for estimating hourly photosynthetically active radiation (PAR) in China by combining geostationary and polar-orbiting satellite data, *Rem. Sens. Environ.* 165 (2015) 14–26.
- [51] S. Chen, H. Ren, X. Ye, J. Dong, Y. Zheng, Geometry and adjacency effects in urban land surface temperature retrieval from high-spatial-resolution thermal infrared images, *Rem. Sens. Environ.* 262 (2021).
- [52] Z. Huang, Y. Yun, H. Chai, X. Lv, The iterative extraction of the boundary of coherence region and iterative look-up table for forest height estimation using polarimetric interferometric synthetic aperture radar data, *Rem. Sens.* 14 (10) (2022).
- [53] S. Yin, K. Zhou, L. Cao, X. Shen, Estimating the horizontal and vertical distributions of pigments in canopies of ginkgo plantation based on UAV-borne LiDAR, hyperspectral data by coupling PROSAIL model, *Rem. Sens.* 14 (3) (2022).
- [54] M. Bilal, A. Mhawish, M.A. Ali, J.E. Nichol, G.D. Leeuw, K.M. Khedher, U. Mazhar, Z. Qiu, M.P. Bleiweiss, M. Nazeer, Integration of surface reflectance and aerosol retrieval algorithms for multi-resolution aerosol optical depth retrievals over urban areas, *Rem. Sens.* 14 (2) (2022).
- [55] S. Li, B. Jiang, J. Peng, H. Liang, J. Han, Y. Yao, X. Zhang, J. Cheng, X. Zhao, Q. Liu, K. Jia, Estimation of the all-wave all-sky land surface daily net radiation at mid-low latitudes from MODIS data based on ERA5 constraints, *Rem. Sens.* 14 (1) (2022).
- [56] X. Zhong, L. Zhao, X. Zhang, J. Yan, P. Ren, Investigating the effects of surface moisture content on thermal infrared emissivity of urban underlying surfaces, *Construct. Build. Mater.* 327 (2022), 127023.
- [57] J. Muñoz-Sabater, E. Dutra, A. Agustí-Panareda, C. Albergel, G. Arduini, G. Balsamo, S. Bousetta, M. Choulga, S. Harrigan, H. Hersbach, B. Martens, D. G. Miralles, M. Piles, N.J. Rodríguez-Fernández, E. Zsoter, C. Buontempo, J. N. Thépaut, ERA5-Land: a state-of-the-art global reanalysis dataset for land applications, *Earth Syst. Sci. Data* 13 (9) (2021) 4349–4383.
- [58] J. Zou, N. Lu, H. Jiang, J. Qin, L. Yao, Y. Xin, F. Su, Performance of air temperature from ERA5-Land reanalysis in coastal urban agglomeration of Southeast China, *Sci. Total Environ.* 828 (2022), 154459.
- [59] D. Rüdiger, R.S. McLeod, W. Wagner, C.J. Hopfe, Numerical derivation and validation of the angular, hemispherical and normal emissivity and reflectivity of common window glass, *Build. Environ.* 207 (2022), 108536.
- [60] L. Gilmour, E. Stroulou, Ortho-photogrammetry for prefabricated energy-efficiency retrofits, *Autom. ConStruct.* 134 (2022), 104082.
- [61] I. Elkhrachy, Accuracy assessment of low-cost unmanned aerial vehicle (UAV) photogrammetry, *Alex. Eng. J.* 60 (6) (2021) 5579–5590.
- [62] K. Liu, A. Wang, S. Zhang, Z. Zhu, Y. Bi, Y. Wang, X. Du, Tree species diversity mapping using UAS-based digital aerial photogrammetry point clouds and multispectral imagers in a subtropical forest invaded by moso bamboo (*Phyllostachys edulis*), *Int. J. Appl. Earth Obs. Geoinf.* 104 (2021), 102587.
- [63] X. Zhong, L. Zhao, J. Wang, H. Zheng, J. Yan, R. Jin, P. Ren, Empirical models on urban surface emissivity retrieval based on different spectral response functions: a field study, *Build. Environ.* 197 (2021).
- [64] B. Fu, P. Zuo, M. Liu, G. Lan, H. He, Z. Lao, Y. Zhang, D. Fan, E. Gao, Classifying vegetation communities karst wetland synergistic use of image fusion and object-based machine learning algorithm with Jilin-1 and UAV multispectral images, *Ecol. Indicat.* 140 (2022), 108989.
- [65] K. Schneider-Zapp, M. Cubero-Castan, D. Shi, C. Strecha, A new method to determine multi-angular reflectance factor from lightweight multispectral cameras with sky sensor in a target-less workflow applicable to UAV, *Rem. Sens. Environ.* 229 (2019) 60–68.
- [66] D. Xiao, Y. Pan, J. Feng, J. Yin, Y. Liu, L. He, Remote sensing detection algorithm for apple fire blight based on UAV multispectral image, *Comput. Electron. Agric.* 199 (2022), 107137.
- [67] K. Ogawa, T. Schmugge, S. Rokugawa, Estimating broadband emissivity of arid regions and its seasonal variations using thermal infrared remote sensing, *IEEE T. Geosci. Remote* 46 (2) (2008) 334–343.

- [68] H.L. Yongqiang Liu, Mamtimin Ali, Huo Wen, Xinghua Yang, Qing He, Estimating surface broadband emissivity of the xinjiang deserts base on FTIR and MODIS data, *IEEE Access* 4 (16) (2016) 4323–4326.
- [69] M. Wang, X. Xu, Z. Yan, H. Wang, An online optimization method for extracting parameters of multi-parameter PV module model based on adaptive Levenberg-Marquardt algorithm, *Energy Convers. Manag.* 245 (2021), 114611.
- [70] K.H. Cheong, J.M. Koh, A hybrid genetic-Levenberg Marquardt algorithm for automated spectrometer design optimization, *Ultramicroscopy* 202 (2019) 100–106.
- [71] M. Baisariyev, A. Bakytzhanuly, Y. Serik, B. Mukhanova, M.Z. Babai, M. Tsakalerou, C.T. Papadopoulos, Demand forecasting methods for spare parts logistics for aviation: a real-world implementation of the Bootstrap method, *Procedia Manuf.* 55 (2021) 500–506.
- [72] L. Doulou, M. Santamouris, I. Livada, Passive cooling of outdoor urban spaces. The role of materials, *Sol. Energy* 77 (2) (2004) 231–249.
- [73] A. Synnefa, T. Karlessi, N. Gaitani, M. Santamouris, D.N. Assimakopoulos, C. Papakatsikas, Experimental testing of cool colored thin layer asphalt and estimation of its potential to improve the urban microclimate, *Build. Environ.* 46 (1) (2011) 38–44.
- [74] C. Georgakis, M. Santamouris, Experimental investigation of air flow and temperature distribution in deep urban canyons for natural ventilation purposes, *Energy Build.* 38 (4) (2006) 367–376.
- [75] K. Niachou, I. Livada, M. Santamouris, Experimental study of temperature and airflow distribution inside an urban street canyon during hot summer weather conditions—Part I: air and surface temperatures, *Build. Environ.* 43 (8) (2008) 1383–1392.
- [76] G.C. Hulley, S.J. Hook, A.M. Baldridge, Investigating the effects of soil moisture on thermal infrared land surface temperature and emissivity using satellite retrievals and laboratory measurements, *Remote Sens. Environ.* 114 (7) (2010) 1480–1493.
- [77] H. Zheng, X. Zhong, J. Yan, L. Zhao, X. Wang, A thermal performance detection method for building envelope based on 3D model generated by UAV thermal imagery, *Energies* 13 (24) (2020) 1–18.
- [78] J. Wang, Q. Meng, K. Tan, L. Zhang, Y. Zhang, Experimental investigation on the influence of evaporative cooling of permeable pavements on outdoor thermal environment, *Build. Environ.* 140 (2018) 184–193.
- [79] FLIR, UAS Radiometry Technical Note, Wilsonville, OR, USA, 2016.
- [80] S.K. Roy, G. Krishna, S.R. Dubey, B.B. Chaudhuri, HybridSN, Exploring 3-D-2-D CNN feature hierarchy for hyperspectral image classification, *Geosci. Rem. Sens. Lett.* IEEE 17 (2) (2020) 277–281.
- [81] A. Synnefa, M. Santamouris, I. Livada, A study of the thermal performance of reflective coatings for the urban environment, *Sol. Energy* 80 (8) (2006) 968–981.
- [82] Y. Wu, Y. Shan, Y. Lai, S. Zhou, Method of calculating land surface temperatures based on the low-altitude UAV thermal infrared remote sensing data and the near-ground meteorological data, *Sustain. Cities Soc.* 78 (2022), 103615.
- [83] S.S. Heinemann, Bastian, Land surface temperature retrieval for agricultural areas using a novel UAV platform equipped with a thermal infrared and multispectral sensor, *Rem. Sens.* 12 (7) (2020) 86–92.
- [84] H. Liang, Q. Meng, Q. Qi, P. Ren, Spatiotemporal interaction between urban heat island and urban-construction indicators on the block scale in autumn in a humid and hot climate, *Sustain. Cities Soc.* 78 (2022), 103638.
- [85] J. Yang, M.S. Wong, M. Menenti, J. Nichol, Study of the geometry effect on land surface temperature retrieval in urban environment, *ISPRS J. Photogrammetry Remote Sens.* 109 (2015) 77–87.
- [86] C.-D. Wen, I. Mudawar, Modeling the effects of surface roughness on the emissivity of aluminum alloys, *Int. J. Heat Mass Tran.* 49 (23–24) (2006) 4279–4289.
- [87] K. Yu, Y. Liu, D. Liu, Y. Liu, Normal spectral emissivity characteristics of roughened cobalt and improved emissivity model based on Agababov roughness function, *Appl. Therm. Eng.* 159 (2019).
- [88] L. Hu, Y. Sun, G. Collins, P. Fu, Improved estimates of monthly land surface temperature from MODIS using a diurnal temperature cycle (DTC) model, *ISPRS J. Photogrammetry Remote Sens.* 168 (2020) 131–140.
- [89] P. Sismanidis, B. Bechtel, I. Keramitsoglou, F. Götsche, C.T. Kiranoudis, Satellite-derived quantification of the diurnal and annual dynamics of land surface temperature, *Rem. Sens. Environ.* 265 (2021), 112642.